UNIVERSITÀ
DI PAVIA

Dipartimento di Fisica “Alessandro Volta”
Corso di Laurea Magistrale in Scienze fisiche

Low-Frequency Spin Dynamics of Thioether-Bridged Cobalt-Dioxolene Complexes

---

Dinamica di Spin a Bassa Frequenza in Composti Tiolati a Base di Cobalto e Diossolene

Tesi per la laurea di:
Martina Foresti

Relatore:
Prof. Giacomo Prando

Correlatore:
Prof. Alessandro Lascialfari

Anno accademico 2024 – 2025

There's plenty of room at the bottom.

Richard P. Feymann, 1959

Contents

Sommario

Con il termine *spin-crossover* si fa riferimento alla modifica, indotta da opportune perturbazioni fisiche, dello stato di spin degli atomi metallici all'interno di un composto molecolare. Quando il metallo può accedere solamente due configurazioni, queste vengono chiamate rispettivamente alto e basso spin. Lo stato del metallo influenza a sua volta lo spin complessivo della molecola.

In alcuni composti, denominati tautomeri di valenza, a base di leganti organici e metalli (principalmente ferro e cobalto), la transizione di *spin-crossover* è guidata dal trasferimento intramolecolare di un elettrone, che si sposta dal legante al metallo in modo reversibile in funzione della temperatura o dell'irraggiamento luminoso.

In questo lavoro di tesi sono stati analizzati tre sistemi a base di cobalto e diossolene con formula chimica $[\mathrm{Co}(\mathrm{Me}_n\mathrm{tpa})]_2(\text{diox-S-diox})(\mathrm{PF}_6)_2\cdot\mathrm{MeOH}$, che differiscono l'uno dall'altro per il numero n di gruppi metile contenuti del gruppo Me_ntpa. Il composto con $n = 0$ verrà denominato riferimento a basso spin (*low-spin*, LS), quello con $n = 3$ ad alto spin (*high-spin*, HS) e quello con $n = 2$ *spin-crossover* (SCO). Per quest'ultimo è infatti attesa la transizione di *spin-crossover* indotta da tautomerismo di valenza, sulla base di studi effettuati in precedenza su molecole simili e contenenti un numero pari a due di gruppi metile.

Abbiamo analizzato i tre composti mediante magnetometria SQUID e risonanza magnetica nucleare. Coerentemente con quanto atteso, abbiamo riscontrato che i campioni HS e LS presentano uno stato di spin indipendente dalla temperatura e caratterizzato da un valore del momento magnetico quadratico medio relativamente grande per il campione HS e molto minore per il campione LS. Il composto di SCO, invece, subisce una transizione estesa in funzione della temperatura fra due stati che non coincidono con quelli dei due campioni di riferimento – almeno nell'intervallo di temperature accessibili ai nostri esperimenti.

Mediante indagini di risonanza magnetica nucleare abbiamo dedotto che alla temperatura $T \simeq 25$ K avviene il popolamento dei livelli energetici elettronici, che induce lo stato magnetico. Il rilassamento della magnetizzazione nucleare è influenzato, a bassa temperatura, da una distribuzione quasi-statica di campi magnetici locali, mentre ad alta temperatura ($T \geq 100$ K) dal paramagnetismo dei campioni.

Abstract

With the term *spin-crossover* one refers to the interconversion, induced by physical perturbations, between a determined spin state of a metal atom inside a molecule and another state. Whenever there are only two accessible configurations, these are referred to as the high- and low-spin states. The spin of the metal affects the overall magnetic state of the molecule in turn.

In some complexes, named valence tautomers and composed of organic ligands and metal atoms (primarily iron and cobalt), the transition is driven by an intramolecular electron transfer: upon temperature variations, an electron can be reversibly transferred from the metal to the ligand, or vice-versa.

In this work, we investigate three compounds whose chemical formula is $[\mathrm{Co}(\mathrm{Me}_n\mathrm{tpa})]_2(\text{diox-S-diox})(\mathrm{PF}_6)_2\cdot\mathrm{MeOH}$, formed by cobalt ions and dioxolene ligands, which differ from each other in the number n of methyl groups inside Me_ntpa. In detail, the sample with $n = 0$ is referred to as the *low-spin* (LS) reference, that with $n = 3$ as the *high-spin* (HS) reference, and that with $n = 2$ *spin-crossover* (SCO). Based on previous papers in which similar compounds containing two methyl groups were characterized, the SCO complex is expected to undergo a valence-tautomeric spin-crossover transition induced by temperature.

We analyzed the three compounds using SQUID magnetometry and nuclear magnetic resonance, discovering that the HS and LS references display a spin state almost independent on temperature, characterized by a very high mean square amplitude of the magnetic moment for the HS sample and much smaller for the LS sample. The SCO compound, instead, undergoes a transition between two spin states, which do not coincide with those of the two reference samples within the explored experimental window.

At $T \simeq 25$ K, both magnetometry and nuclear magnetic resonance measurements indicate the onset of population on the energy levels. Also, at low temperatures, a quasi-static distribution of local magnetic fields drives the relaxation of the nuclear magnetization, which instead is affected by the paramagnetism of the molecules at higher temperature.

Introduction

In this work, the property of some molecular systems to undergo spin crossover induced by valence tautomerism will be analyzed and studied in detail.

With the term *spin-crossover* (SCO) one refers to the switching between different spin states of a metal atom within a molecule induced by physical perturbations. Whenever there are only two accessible states, these are called the high- and low-spin.

In some complexes, such as the valence tautomers (VT), the transition is driven by an intramolecular electron transfer between a redox-active ligand and the metal atom. The charge redistribution is reversible and it can be modified through external stimuli, which include temperature and pressure, light irradiation (only at cryogenic temperature) and the application of a magnetic field.

The most studied VT materials are based on cobalt and iron metals; in this work we investigate $[\mathrm{Co}(\mathrm{Me_2tpa})]_2(\mathrm{diox\text{-}S\text{-}diox})(\mathrm{PF_6})_2\cdot\mathrm{MeOH}$, which displays cobalt metals and redox dioxolene ligands. At low temperatures, the metal is expected to be in a low-spin state, making the molecule diamagnetic, while at high temperatures cobalt is reduced, acquires a high spin, and the molecule becomes paramagnetic.

We provide a study of the static and dynamic magnetic properties of the compound by means of SQUID magnetometry and pulsed nuclear magnetic resonance (NMR). The SQUID data provide information on the magnetic susceptibility χ as a function of temperature and the magnetization M as a function of the magnetic field H at a fixed temperature. On the other hand, through NMR, we quantify the relaxation times T_1 and T_2 and spectra of the ^{1}H nuclear magnetization at a fixed external magnetic field while varying the temperature.

We compare the results obtained with those of two reference compounds, whose spin state should be fixed over the total investigated temperature range. These are slightly different in chemical composition with respect to the first sample, as the Me_ntpa ligand contains a different number of methyl groups. In detail, while $n = 2$ in the spin-crossover compound, the others display $n = 0$ and $n = 3$.

In the first chapter, we introduce the spin-crossover phenomenon in valence tautomers, and focus on the samples analyzed in this thesis. The second chapter describes the experimental setups and methodology. Finally, the third and fourth chapters summarize the data acquired during SQUID and nuclear magnetic resonance experiments.

Chapter 1

Spin-Crossover in Valence Tautomeric Cobalt Compounds

In this chapter, we describe the main physical properties of the molecular systems studied in this thesis. These are three Cobalt-dioxolene compounds distinguished by the number of methyl groups within the molecule, and one of them is a valence tautomer which undergoes a spin-crossover transition.

Thus, a detailed analysis of the spin-crossover phenomenon will be presented, with a focus on the transition in valence tautomers. Following this, we provide a comparison of some Cobalt-based valence tautomers and conclude with the preliminary characterization of our compounds.

Contents

1.1 The Spin-Crossover Transition

In recent years, the possibility for some materials to exist in two different and equally stable magnetic states (magnetic bistability) has become of wide interest in the framework of molecular-based quantum information processing and spintronics[1]. Even more appealing is the possibility of modifying such magnetic state and tuning the transition in a reversible manner, in order to encode a (qu)bit and control its state.

In this perspective, to date, many molecular-based switchable paramagnetic units have been intensively investigated for the possibility to become sensors and units of storage and processing of digital information. Particular interest is devoted to mixed-valence systems, spin-crossover (SCO) compounds and valence-tautomers[2].

Spin-crossover compounds are formed by metal atoms and organic ligands. The term "spin-crossover" refers to the interconversion between two spin states of the metal ion(s), which in turn affects the magnetic state of the overall molecule. The vast majority of complexes that exhibit SCO displays a central atom of Iron, but other $3d$ transition metals as well can form SCO complexes, and these include Cobalt, Manganese and Chromium[3].

The spin-crossover phenomenon arises because, responding to some external stimuli, the bond length between atoms inside a manifold changes as a result of elastic interactions. In particular, at low temperatures, the bond length between metal and ligand is shorter than it is at high temperatures[4].

From an energetic point of view, if we consider a metal atom inserted into a molecular manifold – which, in most SCO compounds, is tetrahedral or octahedral –, the initially degenerate d orbitals (Fig. 1.1) must reorganize in a doublet (E_g) and a triplet (T_{2g})[5, 6, 7]. Whether the doublet is bonding or antibonding depends on the specific metal and the ligand field strength, induced by geometry. See, for instance, Fig. 1.2, where two different coordinations in a cubic geometry are reported.

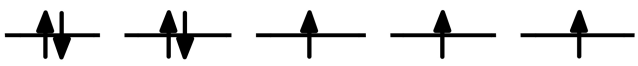

Figure 1.1: The five degenerate d orbitals of a free atom of Cobalt.

However, when considering the entire molecule, the ligand orbitals need to be taken into account and the electrons must rearrange to occupy all the molecular energy levels. If the energy difference between the molecular orbitals is small compared to the energy required to pair electrons in the lowest lying levels – which is a situation typically occurring at high temperatures – the electrons will be more likely to respond to Hund rules and go into higher orbitals maximizing the overall spin instead of pairing

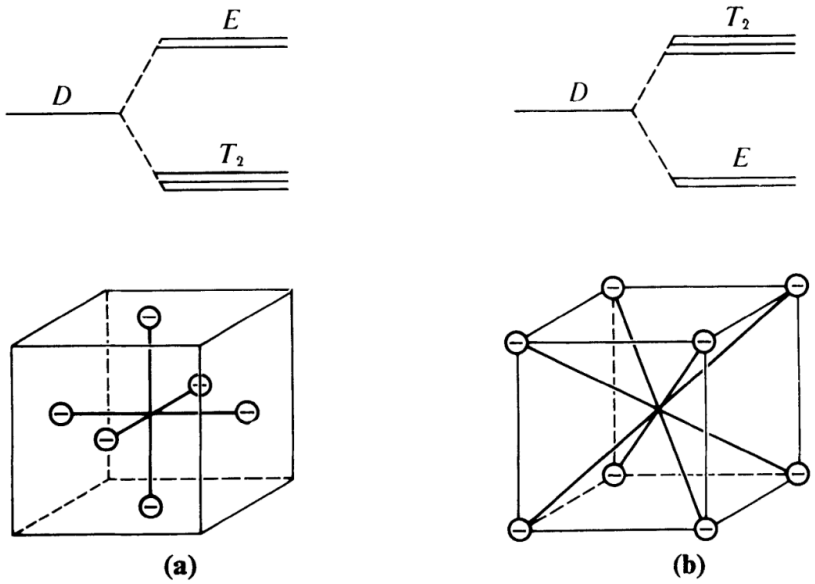

Figure 1.2: The five degenerate *d* orbitals reorganize in a doublet (E) and a triplet (T_2), whose splitting depends on the metal and ligand field strength. The splitting is depicted in the representative case of a crystal field with cubic symmetry and a) sixfold coordination and b) eightfold coordination. Reproduced from Ref. [6].

on the same orbital. As a result, a high-spin situation is reached. However, if the orbital splitting energy is sufficiently large, the electrons will remain in the lowest-lying levels, pairing with anti-aligned spin, thus leading to a lower spin state[7].

When the electrons can access only two possible configurations, these are called the "high-spin" (HS) and "low-spin" (LS) states. From entropy considerations, the low-spin is the electronic ground state at low temperatures (minimum disorder), whereas the high-spin state is easily reached at higher temperatures.[8] As above mentioned, the spin-crossover is associated with changes in the structural properties and interatomic distances. To give an example, some typical distances found with crystal structure analysis in LS and HS materials are $\Delta_r = r_{HS} - r_{LS} \approx 0.18$ Å to 0.2 Å in Iron complexes and $\Delta_r = r_{HS} - r_{LS} \approx 0.07$ Å to 0.11 Å in Cobalt complexes[3].

The interconversion between the two spin states can be driven by some external stimuli, for example the temperature, the application of a magnetic field[9], and even light irradiation. In 1984, P. Gutlich and J. Jung reported a thermal spin-crossover occurring at very low temperatures (≤ 20 K) exploiting light at different wavelengths ($\simeq 550$ nm to excite and $\simeq 880$ nm to deexcite)[4].

The transition can even be tuned through the chemical properties of the substrate on which the molecules are deposed[10]. In addition to this, it may be influenced by the chemical modification of the compound (ligand replacement or substitution), metal

dilution, crystal defects, mechanical treatment and mechanical pressure, together with all the cooperative interactions which occur whenever the molecules are embedded in a crystal lattice (e.g. Jahn-Teller effect).[4, 10, 11]

Essentially, two typologies of SCO in solids are distinguished: a continuous transition, which may be gradual or abrupt within a few Kelvin, and a discontinuous one characterized by hysteresis[4]. A sketch of the phenomenology associated with the different kinds of spin-crossover transition is reported in Fig. 1.3.

When the transition is abrupt, the critical temperature (T_{SCO}) at which it occurs can be defined[8]. According to the Boltzmann distribution:

$$\frac{N_1}{N_2} = \exp\left(-\frac{E_{HS} - E_{LS}}{K_B T_{SCO}}\right) \tag{1.1}$$

where E_{HS} and E_{LS} are the fixed energies of the high and low spin states.

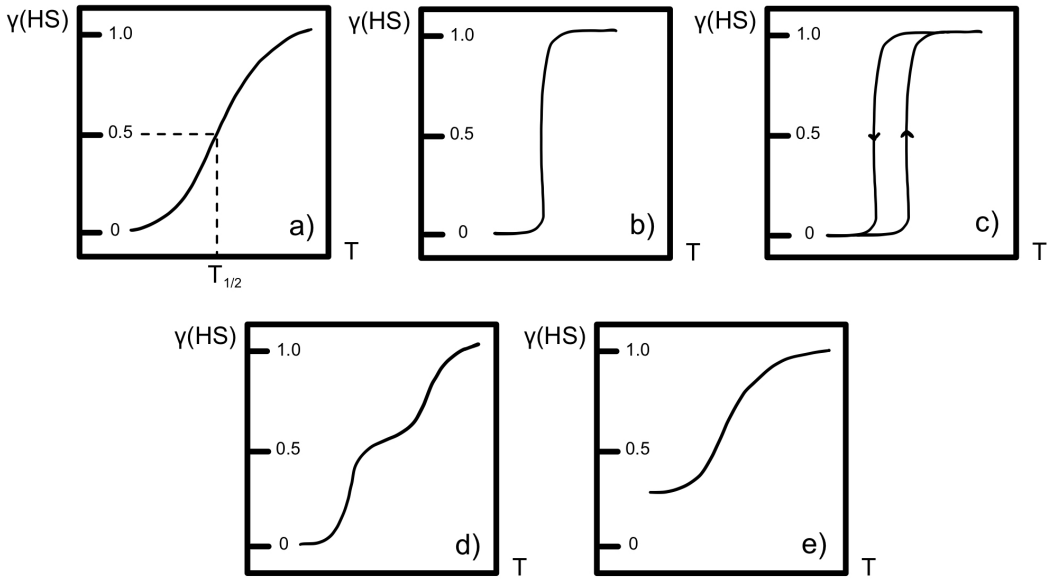

Figure 1.3: Schematic representation of typical spin transition curves of the molar fraction of HS nuclei γ_{HS} as a function of temperature T. In detail: a) gradual transition, b) abrupt, c) with thermal hysteresis, d) multiple switching, e) with HS residual. Adapted from Ref. [4].

Alternatively, some complexes can experience multiple switching, accessing intermediate states between the low- and high-spin states. This happens mostly in dilute systems such as liquid or rigid solutions, doped crystalline materials and complexes where symmetry breaking can lead to two or more inequivalent metallic centers[12].

Spin-crossover was first discovered in Iron complexes and it has been extensively investigated in these compounds ever since[3, 4, 13]. One of the reasons is the large number of molecules and crystalline geometries containing Fe(II) and Fe(III) which undergo this type of transition, most of which have a tetrahedral, octahedral or pseudo-octahedral geometry. Examples concerning other metal ions and, in particular, Cobalt are rarer.

Compared with Iron complexes, the Cobalt-based ones are known to display a more gradual transition[3, 10, 14]. In addition to this, some of them have attracted interest for their thermal hysteretic behavior, that is, the compound recalls its thermal history and different trends arise in response to the same thermal conditions.

One of the first examples of such systems was investigated by J. Zarembowitch and O. Kahn by means of magnetometry and electron paramagnetic resonance spectroscopy[15]. In particular, they discovered a gradual, hysteretic, complete interconversion, extending from $T = 20$ K to $T = 295$ K.

Indeed, magnetometry is a very powerful experimental technique to determine the occurrence of a SCO transition. In particular, the SQUID apparatus can measure the magnetic susceptibility χ_M of a sample as a function of the temperature. For a paramagnetic compound, χ_M follows a Curie-Weiss behavior, namely

$$\chi_M(T) = \frac{ng^2\mu_B^2 S(S+1)}{3k_B T} \tag{1.2}$$

where μ_B is the Bohr Magneton ($1.38 \cdot 10^{-16}$ erg/K), S is the spin quantum number characteristic of the compound, and g is the Landè factor. From this law, in a paramagnet $\chi_M T$ should be constant over a wide temperature range. Therefore, if the magnetic susceptibility changes as a result of a SCO transition, then this trend is not followed anymore.

The magnetic susceptibility multiplied by temperature $\chi_M T$ of the compound by Zarembowitch and Kahn exhibits two plateaus at low and high temperatures, which correspond to the (fixed) LS and HS states, respectively. In addition to this, $\chi_M T$ displays two trends, indicating hysteretic behavior. The original graph from Ref. [15] is reported in Fig. 1.4

Remarkably, Zarembowitch and Kahn reported that appreciable differences in the results were observed if the monitored temperature suffered from fluctuations. Also, in samples arising from separate preparations but with identical chemical formula and infrared spectra, the T_{SCO} and the slopes of the curves near transition were different. The sensitivity of the spin-crossover phenomenon with respect to sample preparation had already been observed by other authors[15, 16, 17].

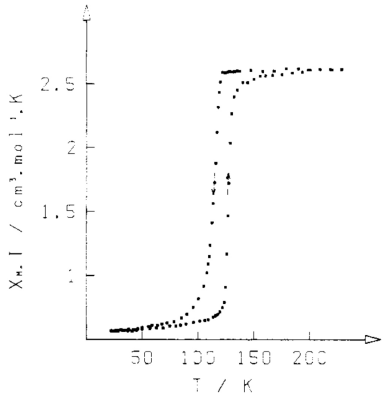

Figure 1.4: $\chi_M T$ vs temperature of $Co(H_2(fsa)_2en)(py)_2$ studied in Ref. [15]. The rising and falling arrows indicate increase and decrease of the temperature, respectively. Also, $T_{SCO}\downarrow = 115$ K and $T_{SCO}\uparrow = 127$ K. Reproduced from Ref. [15].

1.2 Valence Tautomerism in Cobalt Compounds

Valence tautomers (VT) are spin-crossover materials featuring metal ions bounded to redox-active organic ligands. Within this category of materials, the spin-crossover transition is accompanied by an intramolecular electron transfer, which means an electron is transferred from the electronic orbitals of the organic ligand to the electronic orbitals of the metal atom upon application of the physical stimuli mentioned above. The charge redistribution is reversible and can be tuned and controlled at will[8].

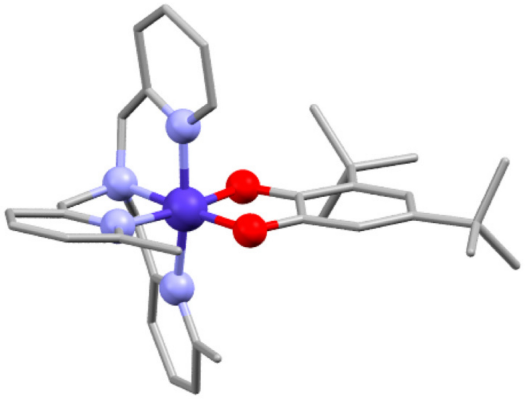

Figure 1.5: Molecular structure of $[Co(Me_2tpa)(DBCat)]PF_6$ where Cat = cathecolato. Ball colors: Cobalt (grey), Oxygen (red), Nitrogen (violet). Carbon is grey stick and hydrogen atoms are omitted for clarity. Adapted from Ref. [9].

The authors of Ref. [9], who analyzed a compound with chemical formula $[Co(Me_2$

tpa)(DB)]PF_6 – where Me_2tpa = bis(6-methyl-(2-pyridylmethyl))amine and DB = 3,5-di-tert-butane – report that when the temperature is low, Cobalt is in a low-spin state and is coupled to the DB ligand in a binegative diamagnetic state, also called *catecolato* (cat) – see Fig. 1.5. Two electrons – one from the ligand and one from the metal – are found to be anti-aligned in the π^* ligand molecular orbital thus the overall molecule is diamagnetic. The geometry is octahedral and the filled T_{2g} orbitals originate short metal-ligand bond lengths with values of $1.9-2.0$ Å[18].

However, an electron from the DB ligand is transferred to the metal upon heating so that the ligand oxidizes to a mononegative state, called *semiquinonato* (SQ). The Cobalt, instead, transitions to a high-spin state, and is ferromagnetically coupled to the magnetic moment of the ligand. The number of unpaired electrons increases, implying that the overall molecule is paramagnetic. Therefore, a VT transition has occurred.

This specific interconversion is shown in Fig. 1.6, but similarly to the compounds which will be analyzed in this thesis, for most valence-tautomeric systems the metal-ligand exhange coupling constant and electronic disposition of orbitals are not known yet, and are often inferred by making comparisons with analogue molecules[19].

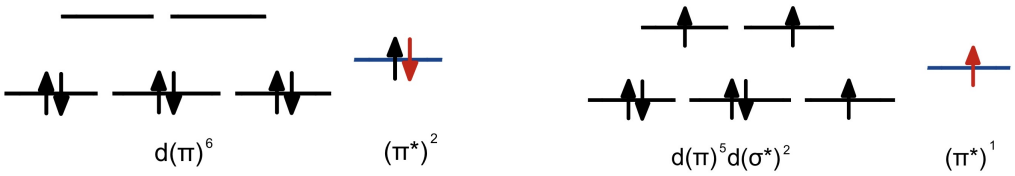

Figure 1.6: Representation of the electronic states associated to the VT-SCO transition in the complex analyzed in Ref. [9]. The low-spin diamagnetic and the high-spin paramagnetic states are shown in the left-hand and right-hand panels, respectively. The atomic orbitals are black; the ligand orbitals blue. Red is for the electron of the ligand. Adapted from Ref. [9].

Some of the most investigated Cobalt-based VT complexes are those that exhibit two *o*-dioxolene (diox) ligands, where a range of thermodynamic criteria governs the nature of the VT transition. For instance, if the Cobalt and dioxolene redox potentials do not match, this leads to a temperature-invariant interconversion. Also, the degree of electronic interaction between the two dioxolene ligands and the metal ion can have a strong influence on the transition[1, 12]. Indeed, if the interaction is too strong, the resulting transition is partial or incomplete (see Fig. 1.3) and its onset is only observed at very high temperatures – e.g. 353 K for the compound discussed in Ref. [20]. On the other hand, a too weak coupling between the metal and ligand leads to a concerted transition.

1.3 Cobalt-Dioxolene Compounds

Modifying the chemical composition can strongly influence the magnetic state of a molecule and, in particular, the increase or decrease of the number of radicals can "freeze" a molecule in a magnetic state which does not change upon application of any external stimulus. In other words, in this case the ligand and the Cobalt have a fixed oxidation state which do not change and a VT transition does not occur.

As a relevant example, Fischer and coworkers studied in Ref. [12] a family of three Cobalt-dioxolene compounds with chemical formula $[Co(Me_ntpa)_2(thM)](PF_6)_2$, where tpa is a tris(2-pyridylmethyl)amine and $n = 0$ (compound **1**), $n = 2$ (**2**), $n = 3$ (**3**) correspond to the number of methyl groups linked to the pyridine rings at their 6-position. In order to obtain single crystals, the authors needed to layer different solutions of the three compounds with organic solvents – a MeCN solution of **1** with toluene; a CH_2Cl_2 solution of **2** with Et_2O (**2a**) or hexane (**2b**) and an acetone solution of **3** with hexane.

Thanks to theoretical models of geometry distortion and theoretical determination of the internuclear bond lengths, the authors were able to determine the oxidation state of the Cobalt centers and ligands.

In particular, at low temperatures the samples **1** and **2** display an octahedral geometry characterized by short Co-O/N bond distances and low distortion, which is consistent with a low-spin Co(III) and a cathecolate ligand (LS-Co(III)Cat). The sample **3**, instead, exhibits elongated bond lengths and its geometry is pseudo-octahedral corresponding to a high-spin Co(II) and semiquinonate ligand (HS-Co(II)SQ).

Upon increasing the temperature and eventually reaching ambient conditions, the compounds **1** and **3** persist in their oxidation states, whereas **2a** and **2b** show X-ray absorption spectroscopy bands compatible with a HS state of the Cobalt ion. Therefore, the latter undergo a VT spin-crossover transition while the **1** and **3** samples have a fixed oxidation state of their components at all temperatures.

The data of SQUID measurements of $\chi_M T$ as a function of temperature lead to the same conclusions found with X-ray absorption spectroscopy. We report in Fig. 1.7 what the authors of [12] obtained from SQUID analysis of their samples.

Through magnetometry, the authors could infer the magnetic state of the three compounds, identifying the high and almost temperature-independent value of $\chi_M T \simeq 5.6/6.0$ $cm^3mol^{-1}K$ of the sample **3** as a high spin of the overall molecule. This arises following an initial population of excited states in the HS-Co(II) moiety at $T \simeq 25$ K. The same holds for the compound **1**, where the very low value of $\chi_M T \simeq 0.0 - 0.05$ $cm^3mol^{-1}K$ unveils a temperature-invariant LS-Co(III)Cat charge distribution.

The VT-SCO transition of the samples **2a** and **2b** is accompanied by low values of $\chi_M T$ at low temperatures, and $\chi_M T \simeq 3.8 - 4.0$ $cm^3mol^{-1}K$ at 400 K. The initial and final spin states do not coincide with those of the two reference samples, and moreover the transition is incomplete, which means that plateaus at high or low temperatures

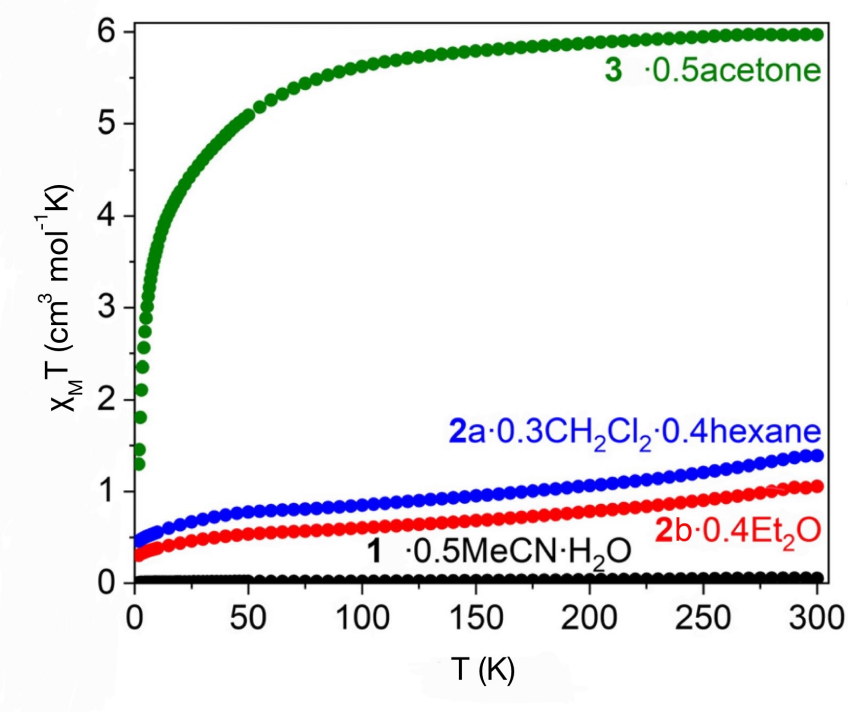

Figure 1.7: Plots of the $\chi_M T$ vs T between $T = 1.8$ K and $T = 300$ K of the compounds **1** (0.5MeCN ·H_2O), **2a** (0.3CH_2Cl_2 ·0.4hexane), **2b** (0.4Et_2O) and **3** (0.5acetone). Adapted from Ref. [12].

are not observed.

In order to determine the fraction of LS nuclei that have interconverted, the ratio of $\chi_M T$ was calculated: the results show $\simeq$ 60 % and 70 % for the samples **2a** and **2b**, respectively.

The methylation at 6-position of the tpa ligand leads to a SCO transition even if the material is not based on dioxolene ligands. For example, the compound of Ref. [9] has chemical formula [Co(Me_2tpa)(DBCat)](PF_6), and coherently with what predicted, the authors report to have obtained a complete VT interconversion ranging from $T = 100$ K to $T = 200$ K, centered at a temperature of 160 K. We show the electronic magnetic susceptibility they measured as a function of the temperature in an applied magnetic field of 0.1 T in Fig. 1.8. Above $T \geq 200$ K, Cobalt is in a known high spin (3/2) state, all molecules are paramagnetic and the susceptibility multiplied by temperature $\chi_M T$ is nearly constant, with $\chi_M T \simeq 2.67$ cm^{3}mol^{-1}K. However, upon decreasing the temperature, some molecules start becoming diamagnetic. There is a molar fraction of molecules which remain high-spin even at low temperatures, and that is the reason why the $\chi_M T$ does not reach net zero: its estimated value is 3.0%.[9]

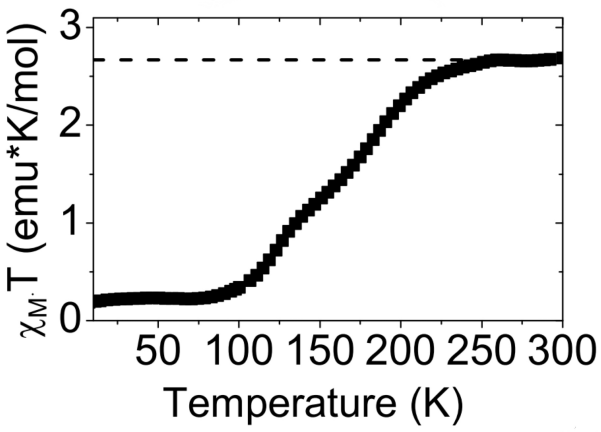

Figure 1.8: $\chi_M T$ vs temperature of [Co(Me_2tpa)(DBCat)](PF_6), for $H = 0.1$ T. The horizontal dashed line refers to the high-temperature plateau $\chi_M T = 2.67$ $cm^3 mol^{-1} K$. Adapted from Ref. [9].

1.4 [Co(Me_ntpa)]$_2$(diox-S-diox)(PF_6)$_2$·MeOH

In this Section, we provide a brief explanation of the synthesis and the preliminary investigation of the compounds that we analyzed experimentally, with chemical formula [Co(Me_ntpa)]$_2$(diox-S-diox)](PF_6)$_2$ ·MeOH.

These molecules consist of three dinuclear Cobalt-dioxolene compounds chemically functionalized with a thioether (solfur) bridge, as shown in Fig. 1.9. The two Cobalt atoms are linked to the bis-dioxolene ligand diox-S-diox – with long formula 6,6'-((1,4-pnehylenebis(methylene)) bis(sulfanediyl))bis(3,5-di-*tert*-butyl-benzene-1,2-diol) – at two symmetric positions with respect to the symmetry axis of the molecule, and are also connected to the tpa (tris(2-pyridylmethyl)amine) ligand. A different methylation ($n = 0, 2, 3$) in the 6- position of the pyridine moieties results in three different manifolds[2].

We received three small jars containing the Cobalt-dioxolene complexes, which are in the form of powder. As shown in Fig. 1.10, the sample with $n = 0$ is light green, while the others are dark green / gray. Their synthesis was carried out by L. Sorace and G. Poneti at the University of Firenze following the steps described in Ref. [2] and Ref. [21].

From now on, we will refer to the compounds with $n = 0$ and $n = 3$ as "low-spin reference" (LS) and "high-spin reference" (HS), respectively, and to the compound with $n = 2$ as "spin-crossover" (SCO). This choice is due to the results attended, based on previous experimental analysis and observations on similar compounds[2, 9, 12]. Also, the color of the compounds is in agreement with what is expected at high temperatures,

as the SCO transition should involve changes of color as well[1].

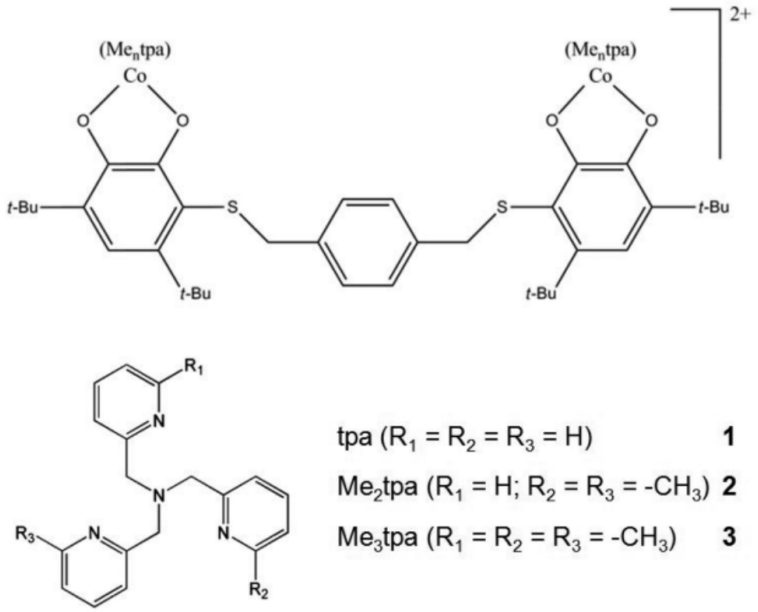

Figure 1.9: Top: schematic representation of the molecular core of the family of complexes. Bottom: tpa ligand with number of methyl groups $n = 0$ (LS reference), $n = 2$ (SCO) and $n = 3$ (HS reference). Adapted from Ref. [2].

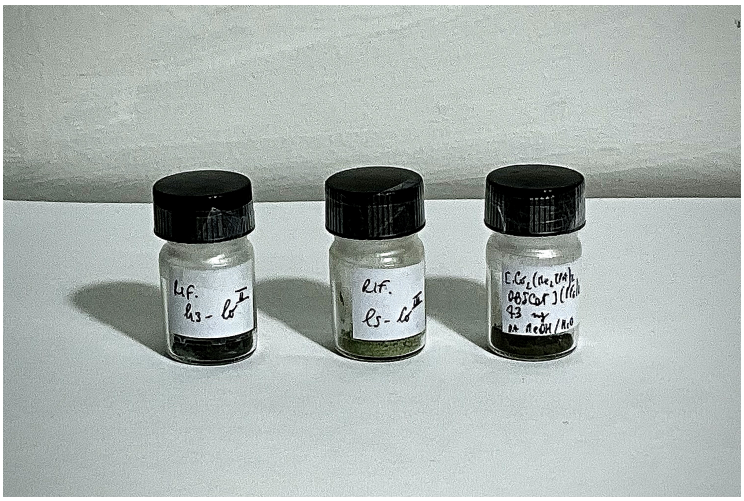

Figure 1.10: Powder samples of $[Co(Me_ntpa)(diox\text{-}S\text{-}diox)Co(Me_2tpa)](PF_6)_2 \cdot MeOH$, where LS is in the center; the SCO sample is on the right and the HS sample is on the left.

Based on preliminary arguments, the LS-Co(III)Cat should have a net spin zero, because apparently the electronic spin of the Cobalt is antiparallel to that of the catecholate ligand. On the other hand, in the HS-Co(II)SQ moiety the Cobalt should have a spin 3/2, parallel to that (1/2) of the semiquinonate ligand. In general, in Cobalt-dioxolene samples the exchange coupling constant between the metal ion and the ligand is not known[9, 19] and therefore we are not able to conclude what the net spin of the overall molecules is.

Before the experimental investigations, we pressed the powder samples in a more compact form inside plastic and quartz capsules, used for SQUID and nuclear magnetic resonance, respectively, sealing the capsules with Teflon tape.

1.4.1 Preliminary Characterization

A preliminary sample characterization of the $[Co(Me_n tpa)]_2(diox\text{-}S\text{-}diox)(PF_6)_2 \cdot MeOH$ samples was reported in Ref. [2] by means of X-ray photoemission spectroscopy and X-ray absorption spectroscopy, as well as magnetometry and photomagnetism. We report the results of X-ray absorption spectroscopy in Fig. 1.11. X-rays can trigger the electronic transitions, leading to an estimate of the electronic configuration also as a function of the temperature.

With reference to Fig. 1.11, the upper and lower trends unveil a charge distribution mostly independent of temperature changes for the **1** (LS) and **3** (HS) compounds. These can respectively be attributed to LS-Co(III)Cat and HS-Co(II)SQ configurations.

On the other hand, compound **2** shows a superposition of signals arising from the two redox isomers at every temperature. Upon cooling, the main peak in the spectrum at $E = 781.5$ eV – associated to the LS-Co(III) – increases in intensity, while the spectral band ($778 - 779$ eV), which represents the HS-Co(II), flattens. This indicates a valence tautomeric interconversion. The data at room temperature were also confirmed by X-ray photoemission spectroscopy, as well as ultraviolet-visible and infrared spectroscopies[2].

Through a spectral deconvolution, the authors managed to define the thermal distribution of HS-Co(II) and LS-Co(III) nuclei, considering the theoretical spectra in the lower part of Fig. 1.11 as limit compositional references. At low temperature, in particular, the percentage of HS-Co(II) is estimated to be 52 %, which is in contrast with that found from SQUID measurements, which is 29%. The authors argue that the difference might be due to the distinct sample preparation as well as the experimental techniques involved in the two cases, which perceive diverse backgrounds.

Also, in Fig. 1.11 a light-induced VT-SCO interconversion is visible through the green line in the center of the figure. This phenomenon is related to SOXIESST effect (Soft X-ray-Induced Excited Spin State) and was previously observed in other Cobalt-dioxolene complexes[4, 9, 10, 23]. In fact, upon application of an infrared laser

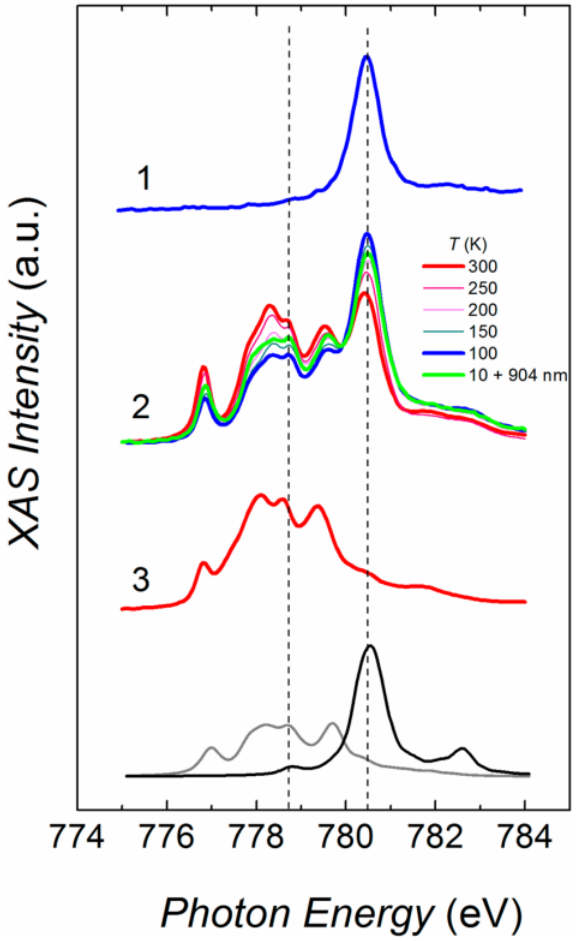

Figure 1.11: X-Ray Absorption spectra of our LS (**1**), SCO (**2**) and HS (**3**) compounds, along with calculated spectra of pure HS-Co(II) (gray line) and LS-Co(III) (black line). Calculations derive from Ref. [22]. Adapted from Ref. [2].

light (wavelength 904 nm), and performing the experiment at cryogenic temperatures, the SCO sample – originally exhibiting mostly LS-Co(III) – shows an increased peak at $E = 780.5$ eV, corresponding to the HS-Co(II) state. The light-induced transition is confirmed through SQUID data, concerning an increase of $\chi_M T$ compatible with a 11 % photo-conversion of the LS-Co(III) to the HS-CO(II) state.

These last data are not available, but we report for the sake of comparison those obtained in Ref. [9]. Here, an infrared laser (940 nm) was coupled to an optical fiber and applied close to the sample. The time of buildup of the magnetic susceptibility under irradiation was studied at a fixed magnetic field intensity ($H = 0.1$ T) and at fixed temperature. The susceptibility χ_M was found to increase with irradiation time

with an exponential law:

$$\chi_M(t) = \chi_0 \left\{ 1 - \exp\left[-\left(\frac{t}{T_{IRR}} \right)^{\alpha_M} \right] \right\} + \chi_1 \tag{1.3}$$

where χ_0 is the light-enhanced magnetic susceptibility, χ_1 is a offset parameter, T_{IRR} is the buildup time and α_M is a stretched exponential. In Fig. 1.12 we report the data obtained at $T = 47$ K, where a clear increase of the magnetization in time is observed.

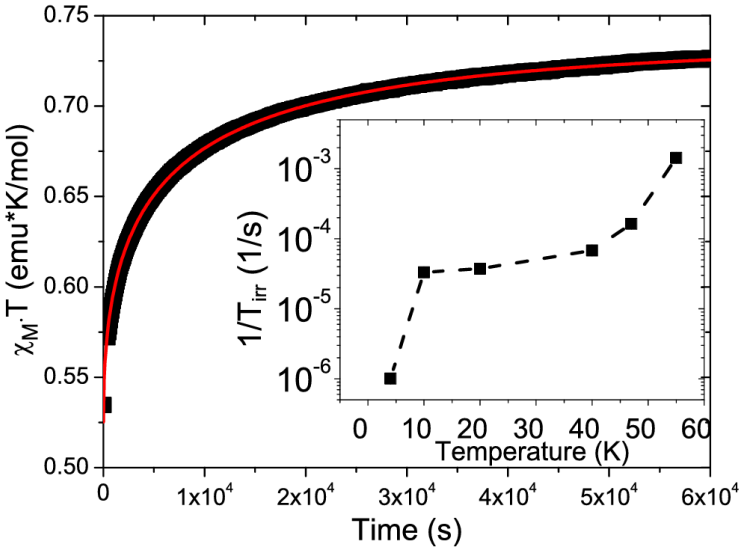

Figure 1.12: $\chi_M T$ vs irradiation time via an infrared laser, at $T = 47$ K in a magnetic field $H = 0.1$ T. The solid line is a best fit according to Eq. (1.2). The inset shows the temperature dependence of the buildup rate. Adapted from Ref. [9].

1.5 Summary

In conclusion, we have analyzed the valence-tautomeric spin-crossover transition induced by temperature variations in Cobalt-dioxolene complexes. We have focused on the three compounds $[Co(Me_n tpa)]_2(diox\text{-}S\text{-}diox)(PF_6)_2 \cdot MeOH$, which display a different number of methyl groups and therefore show different electronic and magnetic states.

In the following chapter, the experimental techniques used for the investigation of these samples will be described in detail.

Chapter 2

Experimental Techniques

Some of the most insightful techniques of investigation of the spin-crossover transition are SQUID magnetometry and Nuclear Magnetic Resonance (NMR).

SQUID (Superconducting QUantum Interference Device) experiments are often the first characterization tool to access the macroscopic magnetic state of a material. NMR, instead, is a powerful spectroscopic method that can provide useful information on the static and dynamic local properties of solids.

In this chapter, we will explore the working principles and experimental setups of SQUID magnetometry and pulsed NMR, focusing our attention on the parameters derived from the two techniques.

Contents

2.1 Nuclear Magnetic Resonance

Nuclear magnetic resonance (NMR) is a spectroscopic technique that exploits radio-frequency pulses, whose frequency ($\simeq$ MHz) is typically low if compared with the characteristic time scales of electronic processes.

NMR takes advantage of nuclear magnetic moments $\vec{\mu}_i$ as microscopic probes for the local fields within the material, which may eventually be superimposed to the external applied fields. The nuclear moments compose the nuclear magnetization

$$\vec{M} = \frac{\sum_i \vec{\mu}_i}{V} \tag{2.1}$$

considering V as the sample volume.

The study of the resonance frequency in NMR spectroscopy can provide useful information on the structural properties, chemical composition and structural disorder of a material (chemical shift)[24]. Additionally, other effects related to the local electronic susceptibility in a conducting sample or a metal (Knight shift) can be deduced from the deviation of the resonance frequency from the bare value defined by the external field.

On the other hand, pulsed NMR protocols make it possible to quantify the relaxation of the nuclear magnetization to thermodynamic equilibrium and to assess the internal dynamics of the samples. This is achieved via the estimate of the relaxation times T_1 and T_2, the latter of which probes the intrinsic coherence time of the statistical system of nuclear spins.

2.1.1 Experimental Setup

We provide a brief description of the typical setup used for NMR experiments (see Fig. 2.1), based on the instrumentation in the NMR laboratory of the Physics Department at the University of Pavia.

The key ingredient of the setup is the probe, which is a radio-frequency transmission line terminating in a resonant LC circuit composed of a solenoidal coil as well as variable and fixed capacitors[25]. The coil generates a pulsed oscillating field $\vec{H}_1$, whose amplitude and time duration are controlled via a TecMag spectrometer connected to a computer. The same coil is also used to inductively detect the NMR output signal, which is then analyzed by the spectrometer. The input and output signals are never mixed thanks to a duplexer.

The sample, suitably encapsulated to fill the coil, is placed inside its turns and fixed with some Teflon tape to ensure electrical insulation during the experiments. When assembling the probe, it is important that the direction of $\vec{H}_1$ is perpendicular to the direction of the external magnetic field $\vec{H}_0$. The latter, in our laboratory, can

be produced by an electromagnet (magnetic field range 0 – 1.8 T) and a cryogen-free superconducting magnet, which can reach up to 9.4 T. Superconductors need to work at temperatures lower than their critical temperature T_c, and, typically, they must be maintained at cryogenic temperatures. For example, in our experimental setup, the coil is made of a TiSn alloy and must be cooled with liquid He because its critical temperature is 9 K.

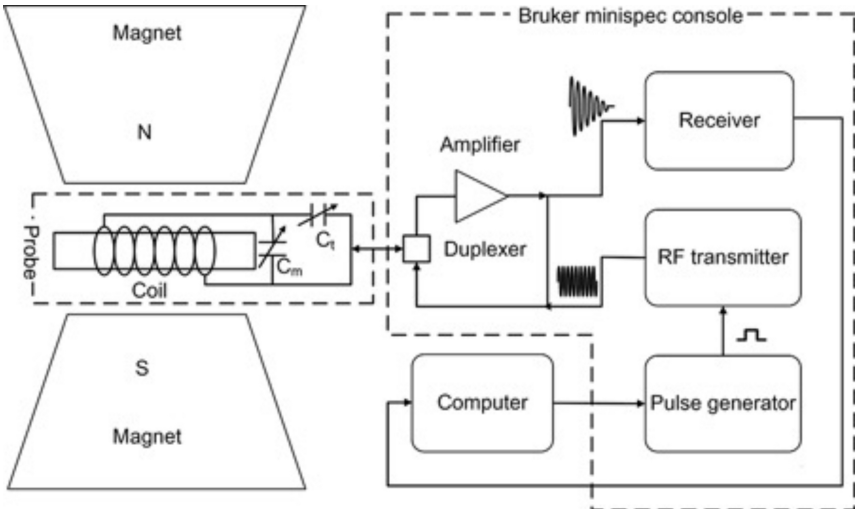

Figure 2.1: Scheme of an NMR setup. Adapted from [26].

The sample as well as the transmission line are inserted in a cryostat which allows to control the temperature. In our experiments, we made use of static flux cryostats, which means that the probe, in the inner part of the device, is in direct contact with helium gas, but not with the cryogenic liquid itself, which instead flows in an outer shell and is pumped through the system from the outside.

The cryogenic liquids often used are liquid nitrogen (N_2), to reach temperatures of 77 K and even $\simeq$ 70 K upon lowering pressure, and liquid helium, which can even reach $T \simeq 2$ K upon lowering pressure. The control over cooling is achieved via an external electronic device, and can be even more precise taking advantage of a calibrated resistive sensor in direct contact with the sample.

2.1.2 Basic Description of the Resonance Process

Every nucleus is characterized by an intrinsic spin angular momentum, named $\vec{I}$ [27]. Referring to the general quantum-mechanical treatment of the angular momentum operators, we can write

$$\hat{I}^2|I,m_I\rangle = \hbar^2 I(I+1)|I,m_I\rangle \tag{2.2}$$

$$\hat{I}_z|I,m_I\rangle = \hbar m_I|I,m_I\rangle \tag{2.3}$$

where $\hat{I}_z$ is the z projection of $\vec{I} = I_x + I_y + I_z$.

The simultaneous eigenstates of $\hat{I}^2$ and $\hat{I}_z$, $|I,m_I\rangle$ are written in terms of the quantum numbers I and m_I. m_I can take $(2I+1)$ values ranging from $-I$ to I in integer steps, and I can take integer or semi-integer values depending on the type of nucleus. However, in order to interact with a magnetic field and produce an NMR signal, the quantum number I of the considered nucleus must be non-zero.

The spin angular momentum $\vec{I}$ is responsible for an intrinsic nuclear magnetic moment $\vec{\mu} = \gamma\vec{I}$, where γ is the gyromagnetic ratio characteristic of the considered nucleus. For instance, the hydrogen isotope ^{1}H – i.e. the proton – has a spin $I = 1/2$ and is characterized by the gyromagnetic ratio $\gamma/2\pi = 42.576$ MHz/T, which grants the proton the most intense magnetic moment, making its NMR signal particularly strong and easy to detect.

Let us therefore consider a proton in an external uniform magnetic field, usually referred to as $\vec{H}_0 = H_0\hat{z}$, whose direction defines the quantization axis $\hat{z}$. A nucleus interacts with the magnetic field $\vec{H}_0$, thus originating a Zeeman Hamiltonian

$$\hat{H}_{\text{Zeeman}} = -\gamma\hbar\vec{I}\cdot\vec{H}_0. \tag{2.4}$$

In the specific case of a proton, the projection of $I = 1/2$ along the z axis can take two values $(\pm\hbar/2)$ which correspond to the parallel and antiparallel state of the spin and are associated with two energy levels, $E = \mp\frac{\hbar\gamma H_0}{2}$. These indicate that the parallel case is less energetic[27, 28].

To undergo transitions between the two states, a nucleus must acquire or lose the energy $E = \hbar\gamma H_0$. As a consequence, whenever subject to an electromagnetic wave with angular frequency ω, the nucleus absorbs the radiation resonantly only if ω is the Larmor frequency:

$$\omega = \omega_L = \frac{\Delta E}{\hbar} = \gamma H_0 \tag{2.5}$$

Classically, a magnetic moment perceiving a magnetic field is subject to a torque $\vec{T} = \vec{\mu}\times\vec{H}_0$ and the resulting motion is a precession with Larmor angular frequency:

$$\gamma(\vec{\mu}\times\vec{H}_0) = \frac{\partial\vec{\mu}}{\partial t}. \tag{2.6}$$

Because the nuclei composing the magnetization $\vec{M}$ have different phase shifts, on average $\vec{M}$ has a null component in the xy plane, whereas $M_z \neq 0$ and its value is related to the different populations of nuclei parallel and antiparallel to the field, $N_\uparrow - N_\downarrow$. At ambient temperature, the aligned component is slightly more populated, due to a Boltzmann factor $\frac{\Delta E}{k_B T} \simeq 10^{-6}$. We then call $M_z = M_0$ the equilibrium value of the magnetization, parallel to the quantization axis (see Fig. 2.2).

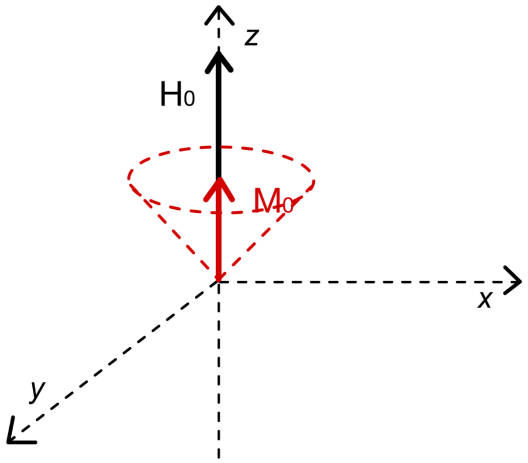

Figure 2.2: Equilibrium state of the magnetization where the net $M_{xy} = 0$, whereas $M_z \neq 0$.

2.1.3 Rotating Frame

During a typical pulsed NMR experiment, the nuclear magnetization aligned to H_0 is driven out of equilibrium using a magnetic field $\vec{H}_1$, lying in the xy plane and oscillating at frequency ω:

$$\vec{H}_1(t) = |H_1| \cos(\omega t). \tag{2.7}$$

Normally, the relation $|\vec{H}_1| \ll |\vec{H}_0|$ holds between the amplitudes of the two magnetic fields[29]. Now, the equation of motion describes a nutation[27]:

$$\gamma \vec{\mu} \times (\vec{H}_0 + \vec{H}_1) = \frac{\partial \vec{\mu}}{\partial t} \tag{2.8}$$

It is not convenient to describe this motion in the reference frame of the laboratory $Oxyz$. In fact, one usually refers to a reference system $Ox'y'z'$ rotating at frequency ω with respect to the z axis of the laboratory frame (see Fig. 2.3).

An oscillating wave like H_1(t) can always be re-written as a sum of two contributions, one rotating clockwise and the other counterclockwise with respect to the $\hat{z}$ axis[27]. Therefore, the overall motion of the magnetic moment in the new frame is a simple precession around a effective field $\vec{H}_{eff}$:

$$\gamma(\vec{\mu} \times \vec{H}_{eff}) = \frac{\partial \vec{\mu}}{\partial t} \tag{2.9}$$

with $\vec{H}_{eff} = \vec{H}_1 + \left(\frac{\omega - \omega_L}{\gamma}\right)\hat{z}$. From this equation, it is clear that if the angular frequency ω corresponds to the Larmor frequency, such as $\omega = \omega_L$, then $H_{eff} = H_1$ and $\vec{H}_1$ in the new frame is stationary and aligned to the $\hat{x}'$ axis. This is called resonance condition. In other words, near resonance, one of the components of H_1 rotates in the same sense as the precession of the moment, and the other component rotates twice as fast, thus can be neglected for the dynamics of the process. As a consequence, in the frame $Ox'y'z'$, a magnetic moment responds only to the field $\vec{H}_1$ and starts precessing with respect to the $\hat{x}'$ axis with angular frequency γH_1.

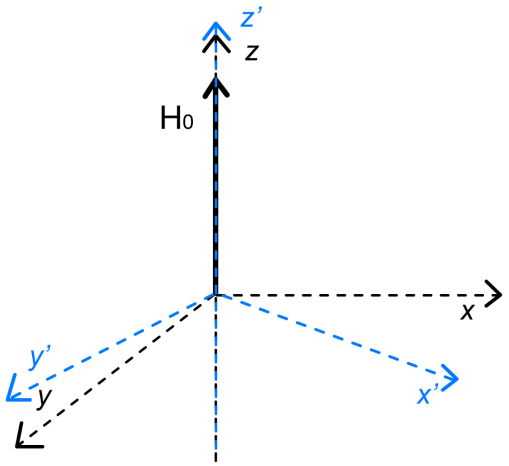

Figure 2.3: The laboratory frame and the new frame representation together with the magnetic field $\vec{H}_0$.

It is then possible to flip the magnetization along a certain direction varying the duration τ of application of the radio-frequency wave and its amplitude. In more detail, the tilting angle is given by

$$\theta = \gamma H_1 \tau. \tag{2.10}$$

Because τ is in general a very short time interval ($\simeq \mu s$), it is usually referred to as a "pulse". Two pulses are noteworthy: the so-called π pulse, which redirects the magnetization upside down, and the $\pi/2$ pulse, which redirects it by an angle 90^o.

2.1.4 Relaxation Times T_1 and T_2

If the magnetic field H_0 was suddenly turned off, then the spins would direct randomly in space. The longitudinal component of the magnetization, which originally has a value $M_z = M_0$, would relax until $M_z = 0$ with an exponential decay with characteristic time T_1. T_1 is referred to as the "longitudinal relaxation time" or "spin-lattice relaxation time".

The recovery of nuclear magnetization towards thermodynamical equilibrium is determined by the time-dependent part of the Hamiltonian, composed of lattice excitations, such as vibrational and molecular motions, and other non-energy-conserving mechanisms, like electronic spin fluctuations[30]. These cause energy transfer from the nuclei to the lattice, and because

$$M_z(t) \propto N_\uparrow - N_\downarrow \tag{2.11}$$

M_z decreases until an equal number of the populations is established.

On the other hand, the relaxation in the transverse plane occurs with a characteristic time T_2, called the "transverse relaxation time" or "spin-spin relaxation time". This involves energy-conserving mechanisms such as hyperfine interactions that redistribute energy among the spins without a net energy change.

Because the processes involved in the two cases are different, T_1 and T_2 may differ by many orders of magnitude, and thus it is possible to perform experiments in which the two times are measured separately.

The overall motion of the nuclear magnetization, which includes the effect of the fields H_0 and H_1, together with the relaxation due to the times T_1 and T_2, is described by the Bloch equations in the $Oxyz$ laboratory frame[30]:

$$\frac{dM_z}{dt} = \frac{M_0 - M_z(t)}{T_1} + \gamma[\vec{M} \times (\vec{H}_0 + \vec{H}_1)]_z \tag{2.12}$$

$$\frac{dM_{x,y}}{dt} = -\frac{M_{x,y}}{T_2} + \gamma[\vec{M} \times (\vec{H}_0 + \vec{H}_1)]_{x,y} \tag{2.13}$$

2.2 Sequences of Radio-frequency Pulses

2.2.1 Free Induction Decay

The minimal pulse that can be applied in an NMR experiment is a $\pi/2$ pulse, used to orient the magnetization along an axis perpendicular to its initial direction.

In the simple case when the magnetization is initially aligned to the $\hat{z}$ axis and is then tilted towards the xy plane by the pulse, it becomes detectable after the pulse by exploiting the law of Faraday-Neumann-Lenz. In particular, the magnetization will evolve in time, precessing in the laboratory frame with an amplitude exponentially decaying in time (with time constant T_2^*), thus generating an inductive electromotive force in the same coil used to create the pulse. This resulting NMR signal is called FID, or Free Induction Decay. Thanks to the quadrature detection within the spectrometer, the FID is acquired in the frame rotating at the working Larmor frequency. The sequence is normally repeated many times in order to improve the signal-to-noise ratio, and a time τ_r is waited before every new start of the sequence (see Fig. 2.4).

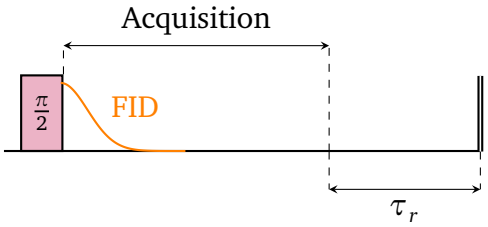

Figure 2.4: Pulsed sequence to detect the FID signal in the time domain.

The rate $1/T_2^*$ is the sum of the effective rate $1/T_2$ of the sample, due to the intrinsic decoherence processes, and the contribution of the spatial inhomogeneities of the magnetic field ΔH_0, such that:

$$\frac{1}{T_2^*} = \frac{1}{T_2} + \gamma \Delta H_0 \tag{2.14}$$

Owing to intrinsic factors like the coil ringing after every pulse, as well as dead times – which need to be waited for the restoring of the circuit –, the FID amplitude is not always easily determined. However, computing the Fourier-transform of the FID,

$$\tilde{I}(\omega) = \int_0^\infty I(t) e^{i\omega t}\, dt \tag{2.15}$$

and considering that:

$$\int_0^\infty \tilde{I}(\omega)\, d\omega = \int_0^\infty \tilde{I}(\omega) e^{-i\omega(t=0)}\, d\omega \tag{2.16}$$

it is finally possible to derive the FID signal amplitude at time $t = 0$, which is proportional to the magnetization present on the xy plane after the application of the last pulse.

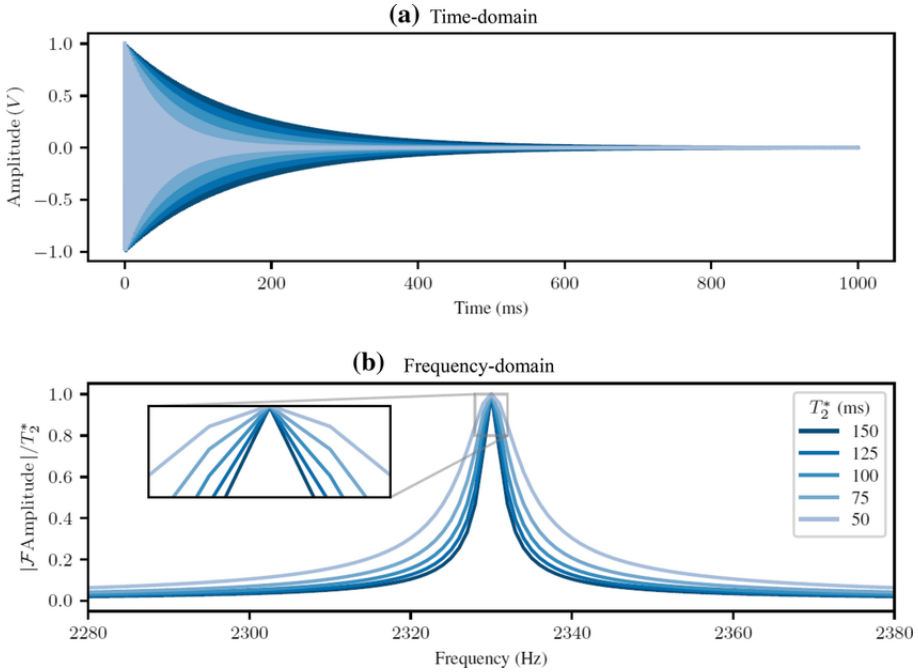

Figure 2.5: FID signals decaying at different T_2^*. Adapted from Ref. [31].

2.2.2 NMR Spectrum

An FID is the time-domain signal obtained after a sequence of radio-frequency pulses. It decays over time, and its analysis is fundamental to derive the frequency-domain spectrum through a Fourier-transform (see Fig. 2.5). To acquire an NMR spectrum, it is essential to irradiate the entire resonance line of the nucleus, as failure to do so results in a point-by-point frequency-swept spectrum. In our case, we were able to irradiate the entire line.

Referring to Fig. 2.6, when observing a hydrogen nucleus, the resulting spectrum is typically centered around the Larmor frequency $\omega_L = \gamma_H H_0$. However, it may be subject to shifts and broadening owing to interactions with other nuclei and electrons.

If the line is homogeneously broadened, then the following equation holds true:

$$\Delta\nu = \frac{1}{T_2 \cdot \pi}. \tag{2.17}$$

which means that the spectral linewidth $\Delta\nu$ is proportional to the value of T_2^{-1}. However, in many solids, the broadening is often inhomogeneous, resulting in a T_2 value decoupled from the linewidth.

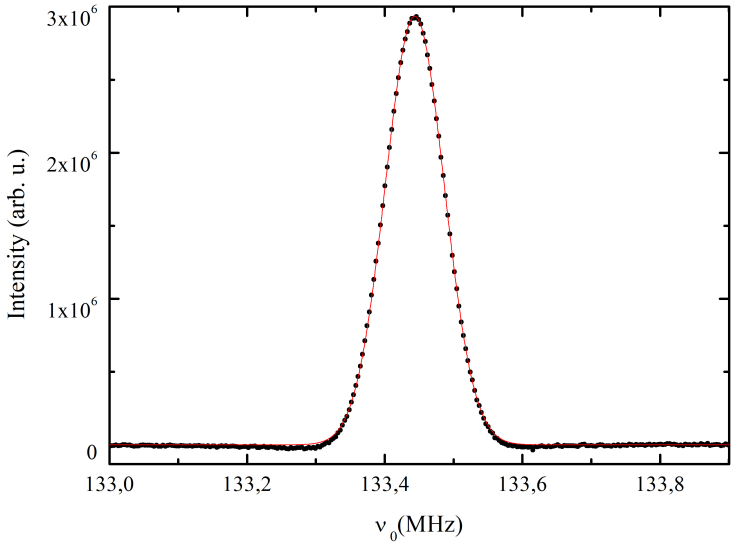

Figure 2.6: ^{1}H-NMR spectrum of the SCO compound in $H = 3.15$ T at $T = 36$ K. The dots are the data and the red curve is their gaussian fit.

2.2.3 Pulse Calibration

The duration of a $\pi/2$ pulse needs to be carefully calibrated before it can be used in experiments. After a calibrated $\pi/2$ pulse, the magnetization is perpendicular to the quantization axis, and the resulting signal acquires its maximum amplitude. Otherwise, if the duration of the pulse is either shorter or longer than the true $\tau_{\pi/2}$, then the magnetization is not completely restored.

This leads to a signal whose amplitude varies as a sine with the pulse duration τ. The curve obtained plotting $I(0)$ as a function of τ can be used to estimate the correct duration of a $\pi/2$ and, by extension, a π pulse. As an example, we refer to the pulse calibration cruve of the HS compound in a magnetic field $H = 1.4$ T at room temperature, shown in Fig. 2.7.

The data obtained were fitted with a damped sine curve, namely:

$$I(0) = A \cdot \sin\left[\left(\frac{2\pi}{T}\right)\tau\right] e^{-(\tau/R)} \tag{2.18}$$

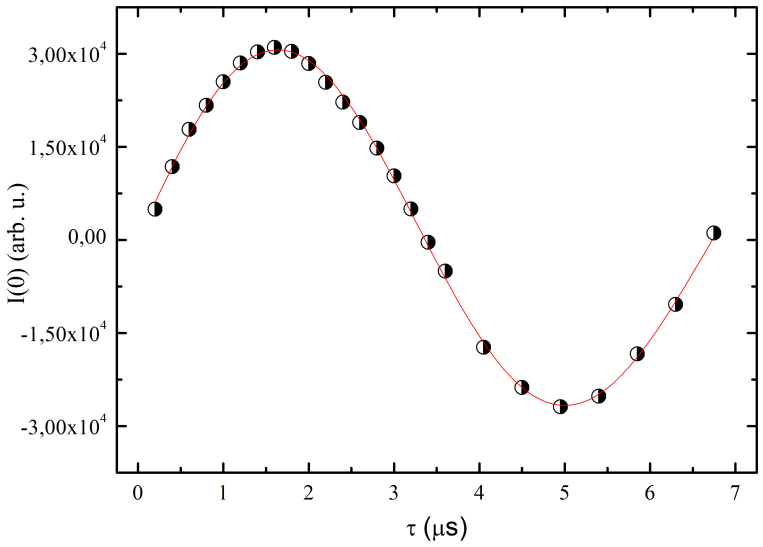

Figure 2.7: Pulse calibration of the HS sample in $H = 1.4$ T at room temperature.

where τ refers to the pulse duration, T is the sine period and R is the decay time during which the amplitude A is reduced by an amount $1/e$. The duration of $\tau_{\pi/2}$ is considered one quarter of the period T. Based on the results in Fig. 2.7, $\tau_{\pi/2} = (1.68 \pm 0.02)\ \mu s$. In general, the higher the intensity of H_1, the shorter the pulse.

2.2.4 Measuring the Spin-spin Relaxation Time

To determine important parameters like the relaxation times T_1 and T_2, it is necessary to define more elaborated pulsed sequences. The most frequent sequences of pulses used to determine T_2 are a "solid echo sequence", composed of two pulses of $\pi/2$ and $\pi/2$ and a "Hahn echo sequence", formed by two pulses of $\pi/2$ and π. In this section we refer to a Hahn echo sequence (see Fig. 2.8).

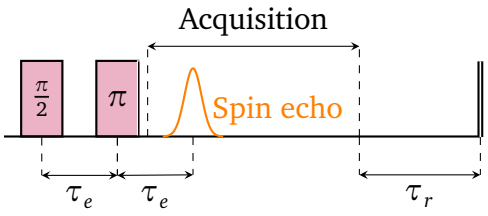

Figure 2.8: Pulsed sequence to detect the Hahn echo signal in time domain.

The preliminary $\pi/2$ pulse is applied to flip the the magnetization from the z axis to the xy plane. Afterwards, a transient time called "echo time" or τ_e is waited. During this interval, due to an inhomogeneity-induced spread of precession frequency[27], some nuclei rotate clockwise and others rotate anti-clockwise (in the rotating frame) and the coherence of the magnetization is lost with an exponential decay with time constant T_2^*. After τ_e, a π pulse is applied to flip the spins thus making them rotate in the opposite direction of their dephasing: this is the central idea of refocusing. If another τ_e is waited, an "echo" signal appears, meaning the restoring of the magnetization. It is remarkable that the shape of the second half of the echo signal is identical to the FID signal.

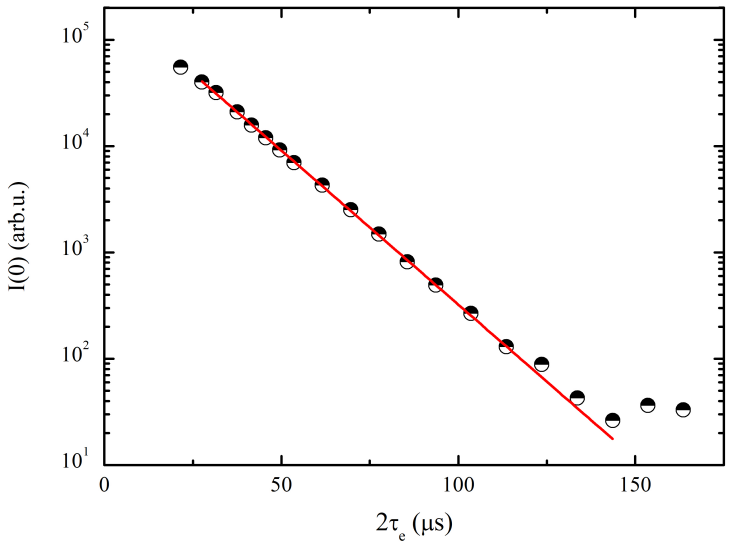

Figure 2.9: $I(0)$ (black) as a function of the delay times $x = 2\tau_e$ of the HS sample in $H_0 = 1.4$ T and at $T = 60$ K, and relative fit (red line).

Now, the numerical fast Fourier-transform of the second half of the echo signal is computed, so that the echo amplitude $I(0)$ is acquired. Because $I(0) \propto M_{xy}$, it diminishes with time constant T_2. Thus, it can be plotted as a function of the delay times $x = 2\tau_{echo}$ for the determination of T_2. The time $x = 2\tau_e$ is an expedient used because the signal appears at even times with respect to this sequence.

As an example, in Fig. 2.9 we report the data $I(0)$ of the HS sample obtained as a function of x in a magnetic field $H_0 = 1.4$ T and $T = 60$ K. The fitting model is as follows:

$$I(0) = A \cdot \exp\left\{-\left(\frac{x}{T_2}\right)^{\beta}\right\} \tag{2.19}$$

where β is a phenomenological stretching parameter that accounts for a distribution of relaxation times T_2 inside the sample.

It is common use to present the values of $I(0)$ in a logarithmic scale, because this makes it possible to judge by eye whether the decay is a mono-exponential or not. In the particular case of Fig. 2.9, the estimated T_2 is $(15.0 \pm 0.1)\ \mu$s.

However, sometimes a stretched exponential gives a value of β which is non-physical ($\beta \leq 0.5$) and can mean that a single exponential hides a different behavior of the nuclei. For example, in certain cases a double exponential of the form:

$$I(0) = A \cdot \exp\left\{-\left(\frac{x}{T_{2,1}}\right)^{\beta_1}\right\} + B \cdot \exp\left\{-\left(\frac{x}{T_{2,2}}\right)^{\beta_2}\right\} \tag{2.20}$$

can also fit the data. This accounts for two inequivalent hydrogen sites which perceive a different environment around them and, as a consequence, relax with different T_2. See, for instance, Fig. 2.10.

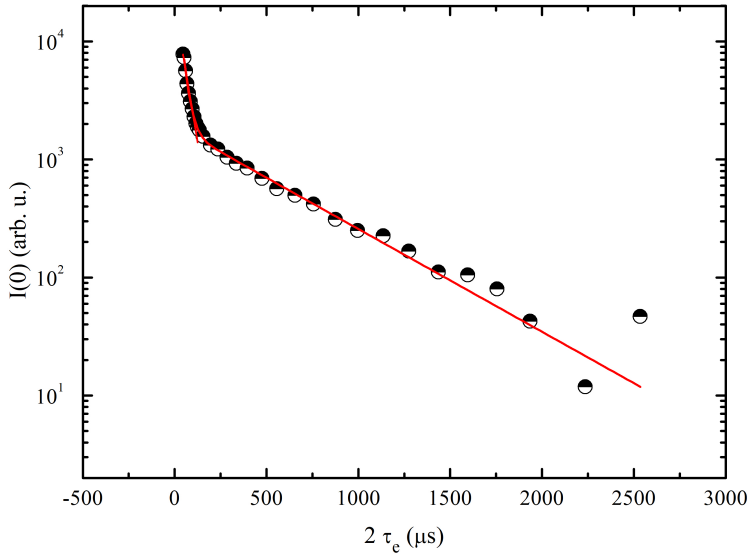

Figure 2.10: $I(0)$ (black) as a function of the delay times $x = 2\tau_e$ of the LS sample in $H_0 = 1.4$ T and at $T = 305$ K, and relative fit (red line).

2.2.5 Measuring the Spin-lattice Relaxation Time

A measurement of the spin-lattice relaxation rate $1/T_1$ can be performed using an inversion spin-echo recovery sequence, which consists of a series of three pulses of π, $\pi/2$ and π (see Fig. 2.11).

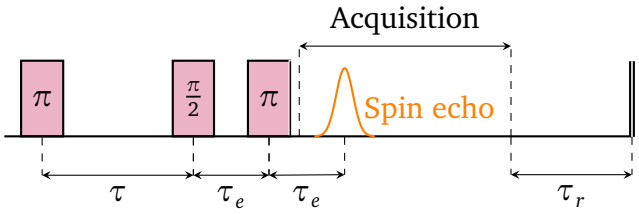

Figure 2.11: Pulsed sequence to detect the recovery of the nuclear magnetization towards the thermodynamical equilibrium in the time domain.

Considering the initial direction of the magnetization along the $+\hat{z}$ axis, and its value as the equilibrium value $M_z = M_0$, after a π pulse it is flipped upside down so as to point towards $-\hat{z}$. Then, a variable delay time τ is waited: during this interval the magnetization relaxes exponentially along the $\hat{z}$ axis with a longitudinal relaxation rate $1/T_1$. In the simple case of a $I = 1/2$ nucleus, the relaxation follows the trend:

$$M_z(\tau) = M_0\left[1 - \exp\left(-\frac{\tau}{T_1}\right)\right] \tag{2.21}$$

After τ, the reading sequence starts, and it can be composed by an echo sequence $(\pi/2 - \tau_e - \pi)$ or a simple $\pi/2$ pulse.

In an echo sequence, a first pulse of $\pi/2$ is applied to switch the remaining magnetization to the xy plane. The situation is now identical as described in Section 2.2.4; following an interval τ_e, a pulse π is applied to refocus the magnetization, and after another τ_e, an echo signal appears. Then, half of the echo signal is Fourier- transformed, integrated and plotted as a function of τ. In contrast to the measurement of T_2, this time the τ values are increased in subsequent measures, whereas τ_e is fixed.

The curve obtained is called the "recovery" of nuclear magnetization, and can be fitted through the following equation:

$$I(0) = y_0 + P_0 \exp\left[-\left(\frac{\tau}{T_1}\right)^{\beta}\right] \tag{2.22}$$

where, again, β is a stretching parameter accounting for a distribution of T_1 values inside the compound, P_0 is proportional to double the amplitude of the magnetization at thermodynamic equilibrium and y_0 is an offset parameter. If the pulses have been calibrated with sufficient care, the curve is symmetric with respect to the x axis. As an example, we report the recovery of the magnetization of the SCO compound in a magnetic field $H = 1.4$ T at $T = 134$ K in Fig. 2.12.

Sometimes, β can also represent inequivalent hydrogen sites which respond to the magnetic field with different relaxation times. In our case, for instance, for the SCO compound at very low temperatures ($T \leq 15$ K) and an external field $H = 1.4$ T, data

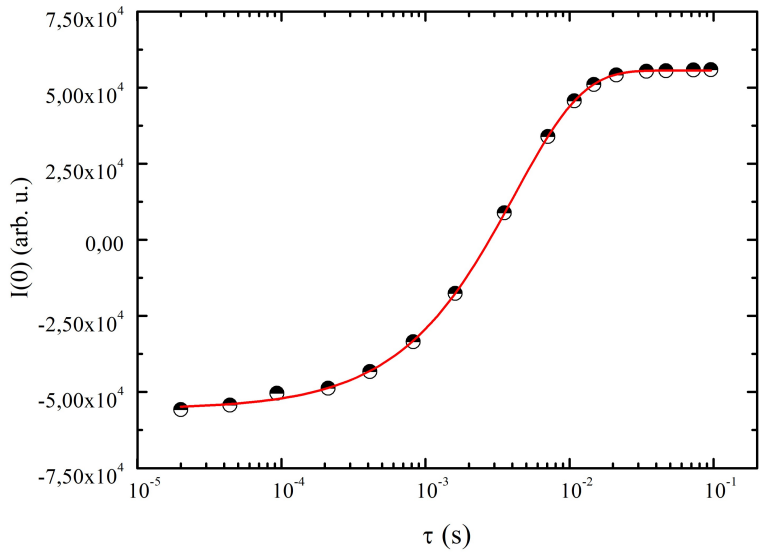

Figure 2.12: Recovery of the nuclear magnetization of the SCO compound in $H = 1.4$ T and at $T = 134$ K. The estimated T_1 value is $T_1 = (4.15 \pm 0.05)$ ms.

were very scattered and somewhat challenging to understand. However, they were nicely fitted with a double exponential with $\beta_1 = \beta_2 = 1$, as reported in Fig. 2.13.

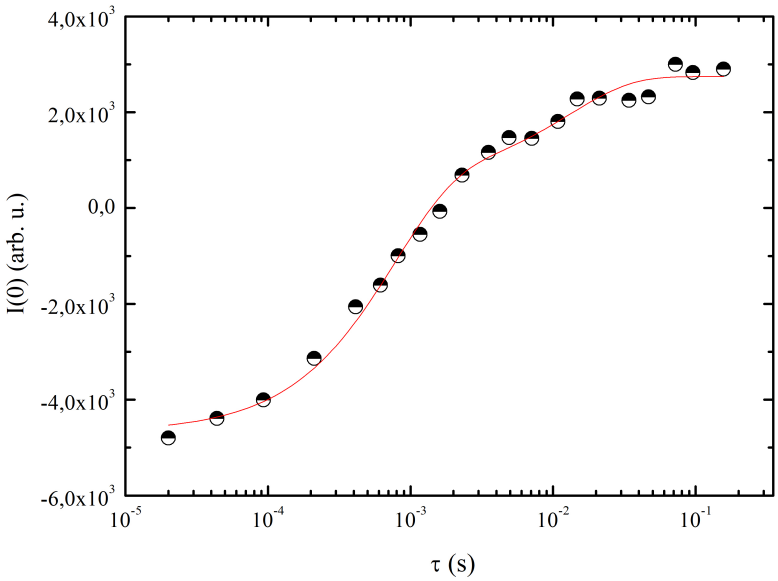

Figure 2.13: $I(0)$ vs τ data of the SCO compound in $H = 1.4$ T and at $T = 12$ K.

2.3 DC SQUID Magnetometry

A SQUID (Superconducting Quantum Interference Device) is a very sensitive magnetometer used to measure extremely subtle magnetic fields. Two other components take part in a SQUID, such as a superconducting magnet, necessary to generate the external magnetic field, and a cryostat.[32]

The magnetometer used in our experiments is a SQUID MPMS-XL7 (Quantum Design) which can act under thermal conditions of 1.8 K $\leq T \leq$ 800 K and fields -7 T $\leq H \leq +7$ T. We indicate with $\pm$ the direction of the field.

Before operation, the powder sample is encapsulated in a straw and placed right at its center to be almost cubic and very small (approximately 5 mm^3) to fill the sample chamber of the magnetometer. Once inserted into the SQUID, and still at room temperature, an insulating vacuum of $\sim 10^{-4}$ mbar is pumped, after which liquid helium flows inside the chamber to obtain the desired temperature for experiments.

The SQUID device is based on parallel superconducting Josephson junctions and it acts as a magnetic flux to voltage converter. In detail, it exploits the Faraday-Neumann-Lenz law and converts in a voltage the changes of flux of magnetic field generated by the sample, as the sample is mechanically moved up and down through a coil.[33] The current induced in the coil is driven through the parallel Josephson junctions, which can interpret the variations of voltage intensity in a value of magnetic moment of the sample. For a better understanding of this mechanism, see Fig. 2.14.

SQUID experiments are often the first characterization method to access the magnetic state of a material[32]. In particular, the fundamental quantity which defines the magnetic identity of a compound is its magnetic susceptibility χ, such as the ratio between the magnetization M of the material and the strength of the external applied magnetic field H

$$M = \chi H \tag{2.23}$$

This relation holds true in the vast majority of experimental conditions, corresponding to high temperatures and low applied magnetic fields.

In general, a SQUID magnetometer is employed to define the static (DC) magnetic properties of solids, whether they are paramagnetic, diamagnetic or become magnetically ordered below a determined temperature, as well as other unconventional mechanisms like superconductivity or the occurrence of a spin-glass[32].

A typical DC SQUID experiment can be performed to study the growth of the magnetization or the magnetic susceptibility of a sample as a function of the temperature in an fixed external magnetic field. In this sense,the measurement can be performed in two ways, called FC (field-cooled) and ZFC (zero-field-cooled), which are, respectively, the measurements undertaken switching the field and then the temperature on or vice versa. Comparison between the results obtained via a FC and ZFC is used to determine whether the state of the material depends on its thermal history. Some

examples are spin-glassy systems and ferromagnets.

Another typology of measurement is the study of magnetization as a function of the external magnetic field, while this ranges from negative to positive values, at a fixed temperature. This is often used to determine hysteresis loops of $M(H)$.

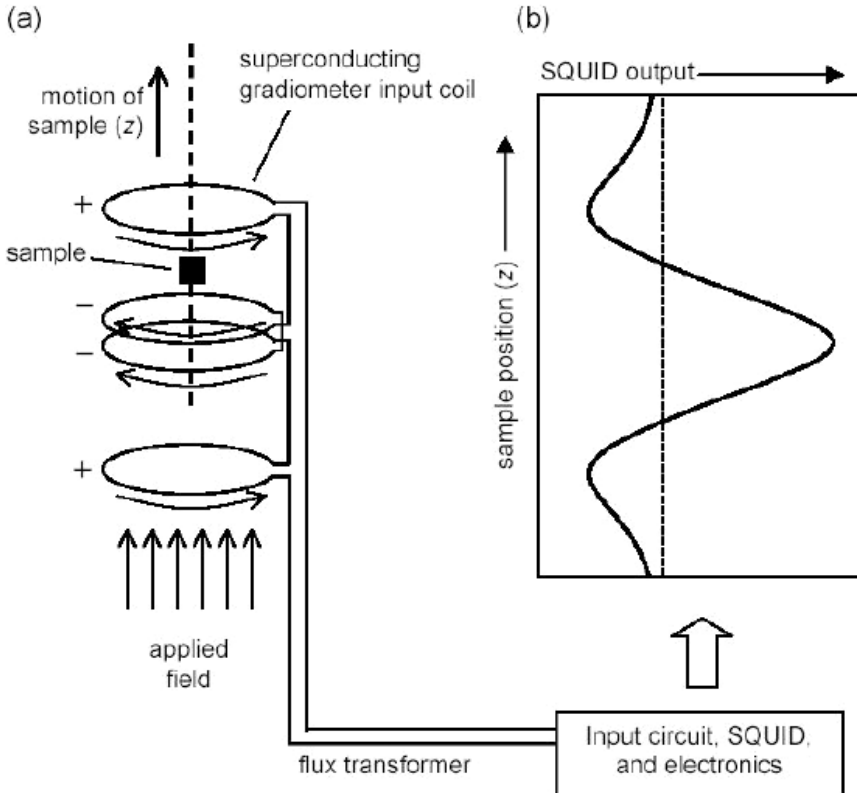

Figure 2.14: a) Scheme of a SQUID magnetometer and b) signal of a SQUID measurement, then converted in a value of magnetization. Reproduced from Ref. [34].

2.4 Summary

In this chapter, we have provided a detailed description of how NMR and SQUID experiments are performed, together with the relevant parameters which will be employed in experiments.

In the following two chapters we show and discuss the results of experiments of pulsed NMR and DC SQUID magnetometry undertaken on the three compounds $[Co(Me_n tpa)]_2(diox\text{-}S\text{-}diox)(PF_6)_2 \cdot MeOH$.

Chapter 3

DC SQUID Magnetometry

This chapter will focus on the macroscopic magnetic characterization of the samples $[Co(Me_ntpa)]_2$(diox-S-diox)$(PF_6)_2$·MeOH ($n = 0$, LS-ref, $n = 2$, SCO and $n = 3$, HS-ref).

We will analyze the data acquired via experiments of DC SQUID magnetometry performed on the three compounds, such as the magnetic susceptibility χ as a function of the temperature at a fixed magnetic field strength, and the magnetization M as a function of the magnetic field, at a fixed temperature.

Contents

3.1 Magnetization vs Temperature

We initially performed field-cooled measurements of the magnetic moment of the three compounds at a fixed intensity of the magnetic field $H = 1000$ Oe. In detail, after the field has been switched on, the temperature is lowered until it reaches 2 K, and then the SQUID captures data of the magnetic moment as the sample is heated by a continuous flow of liquid helium.

The SQUID setup acquires data of the magnetic moment of the overall sample, which comprises the true powder sample, the plastic capsule used to contain the powder, together with Teflon tape used for fixing and also small bubbles of oxygen which may have remained trapped during the encapsulation.

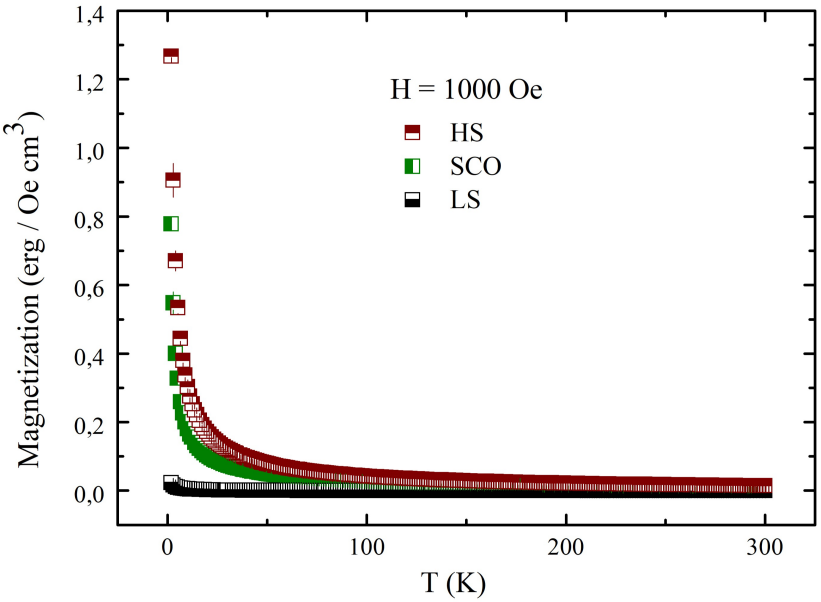

Figure 3.1: Magnetization vs temperature of the HS, SCO and LS samples in $H = 1000$ Oe, without background subtraction.

In Fig. 3.1, data of magnetization as a function of temperature are reported for the three compounds together with their background contribution, which is different for each of them and not easily controlled. Nonetheless, a seemingly paramagnetic response is observed for the three samples, as the magnetization apparently follows a Curie-Weiss behavior $\sim 1/T$. In particular, the values of M are very high for the SCO and HS samples at $T = 1.9$ K, with $M_{HS} = (1.26 \pm 0.4)$ erg Oe^{-1} cm^{-3} and $M_{SCO} = (0.77 \pm 0.04)$ erg Oe^{-1} cm^{-3}, while they are significantly lower for the LS reference, exhibiting $M_{LS} = (2.34 \pm 0.02) \cdot 10^{-2}$ erg Oe^{-1} cm^{-3}. The trends decrease upon increasing temperature, reaching a very similar $M \sim 1 \cdot 10^{-2}$ erg Oe^{-1} cm^{-3}

for the HS and SCO compounds at room temperature, whereas the LS data become negative, with a value $M_{LS} = (-3.46 \pm 0.01) \cdot 10^{-4}$ erg Oe^{-1} cm^{-3}.

Compared to those of the SCO and HS samples, the M data of the LS reference are smaller by more than two orders of magnitude. Also, they pass through zero and change sign at $T \simeq 120$ K and keep decreasing towards negative quantities in the temperature range 120 K $\leq T \leq$ 300 K. For a better comprehension of the phenomenon, we report a zoom-in of the $M(T)$ data of the LS sample alone in Fig. 3.2.

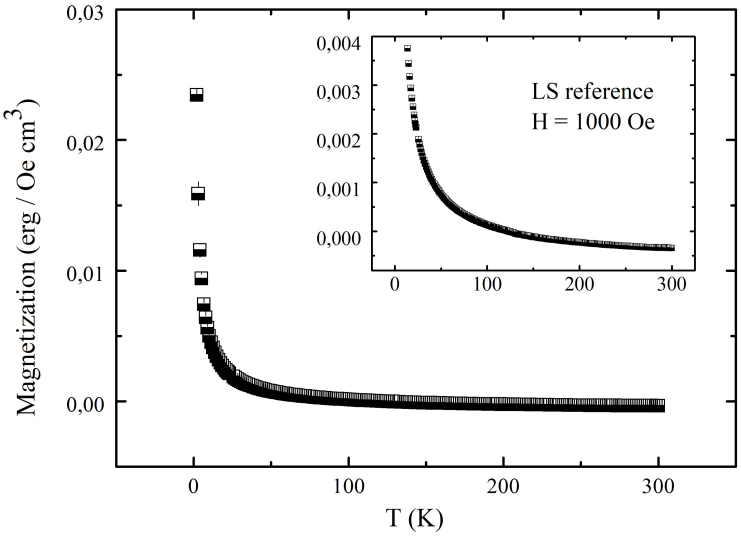

Figure 3.2: Magnetization vs temperature of the LS sample in $H = 1000$ Oe, without background subtraction. The inset is an enlargement highlighting the sign change at $T \simeq 120$ K.

The data of the LS sample can be interpreted as follows. An initial assumption is that the compound does truly display a small and negative value of the magnetic moment – and, by extension, the magnetization – which would account for a diamagnetic behavior. This means that a subsequent plot of the magnetization as a function of the magnetic field would lead to a $M \propto (-H)$ evolution.

In contrast with this hypothesis, the authors of Ref. [2] discovered that the LS reference displays a $\chi_M T$ positive, very small and almost independent on temperature variations, which apparently accounts for a paramagnetic behavior. Indeed, the signal of this compound is very weak, which might be the reason why in our experiments it is easily overcome by spurious contributions, e.g. the background signal from the sample holder. We will quantify this contribution in the next Section.

3.2 Background Contribution

To provide a detailed analysis of the background apparently overcoming the LS-reference data, some measurements of magnetic moment as a function of temperature were carried out on the sample holder alone.

This, in the first instance, is made up of the plastic capsule, used to contain the powder, the Teflon tape used for encapsulation, and also small bubbles of oxygen which may have remained trapped during the process.

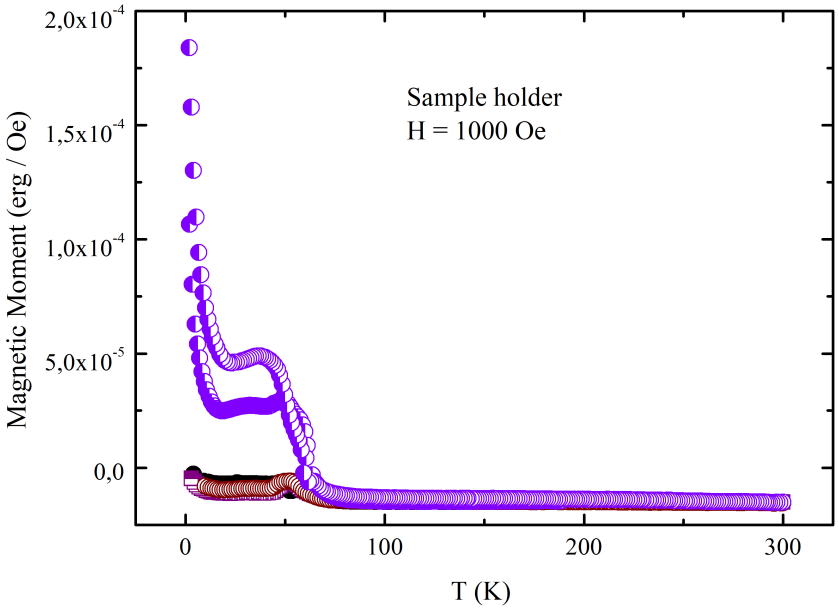

Figure 3.3: Different background contributions acquired at $H = 1000$ Oe.

Referring to Fig. 3.3, after an initial decrease at $T \leq 20$ K, some kinks appear in all the patterns in the same temperature interval ($40 \leq T \leq 55$ K). Above $T \simeq 55$ K, the tendency is negative and seemingly constant. Thus, apparently the shape of $\mu(T)$ is the sum of two contributions: the first, negative and almost constant as a function of temperature, is associated with the capsule and Teflon tape; the latter is attributed to molecular oxygen O_2, whose quantity is not known.

Indeed, the kinks and the subsequent steep decrease of the data are easily explained considering that molecular oxygen undergoes an antiferromagnetic transition at $T \simeq 45$ K, and is strongly paramagnetic at higher temperatures[35]. The transition results in a peak, which is more or less pronounced owing to the quantity of oxygen trapped – in some cases, see, for instance, the violet points in Fig. 3.3, more oxygen

was certainly present. The strong decrease of μ above $T \simeq 50$ K is consistent with a major paramagnetic behavior of this molecule.

Also, the red, purple and black points were acquired after a thorough oxygen decontamination. Although some residual kinks are still visible $T \simeq 50$ K, indeed the negative tendency of the capsule and Teflon tape is in this case more evident.

Taking these analysis into account, we can estimate the background contribution to be subtracted from the samples' data. Considering that the quantity of oxygen is unknown, but still, the encapsulation of the compounds was carried out under controlled conditions to minimize oxygen contamination, we can assume that the background contributes with a negative value of $\mu \simeq (-14.6 \pm 0.5) \cdot 10^{-6}$ erg Oe^{-1} approximately independent on temperature. Thereafter, we reanalyzed the LS reference data applying a subtraction of the background signal.

As evident from Fig. 3.4, a seemingly paramagnetic behavior of this compound is confirmed. Still, the signal intensity is very weak, and this is the reason why it was easily overcome by the spurious contributions of the capsule and Teflon tape, mostly at high temperatures.

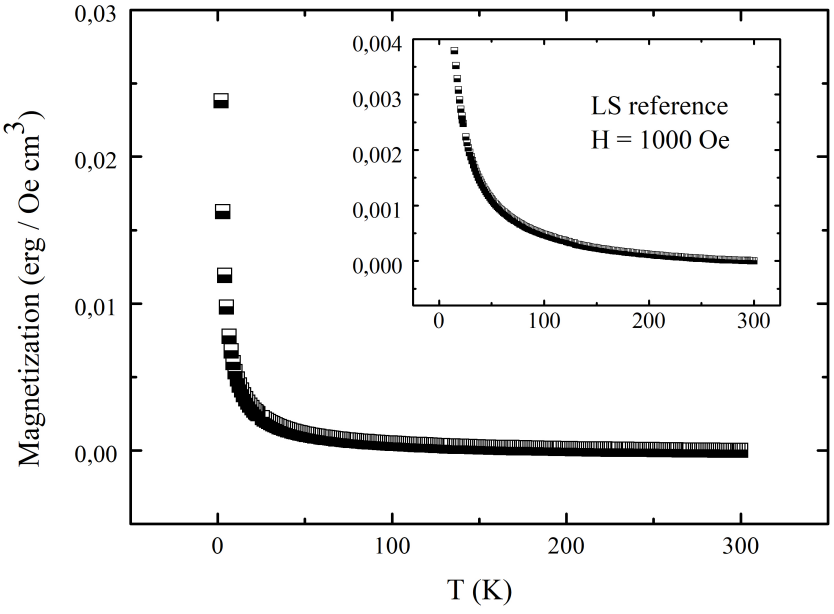

Figure 3.4: Magnetization vs temperature of the LS sample in $H = 1000$ Oe, with background subtraction.

3.3 χT vs Temperature

In Fig. 3.5 the data of magnetic susceptibility multiplied by temperature are reported for the HS, SCO and LS compounds as a function of temperature, at a fixed applied magnetic field intensity $H = 1000$ Oe.

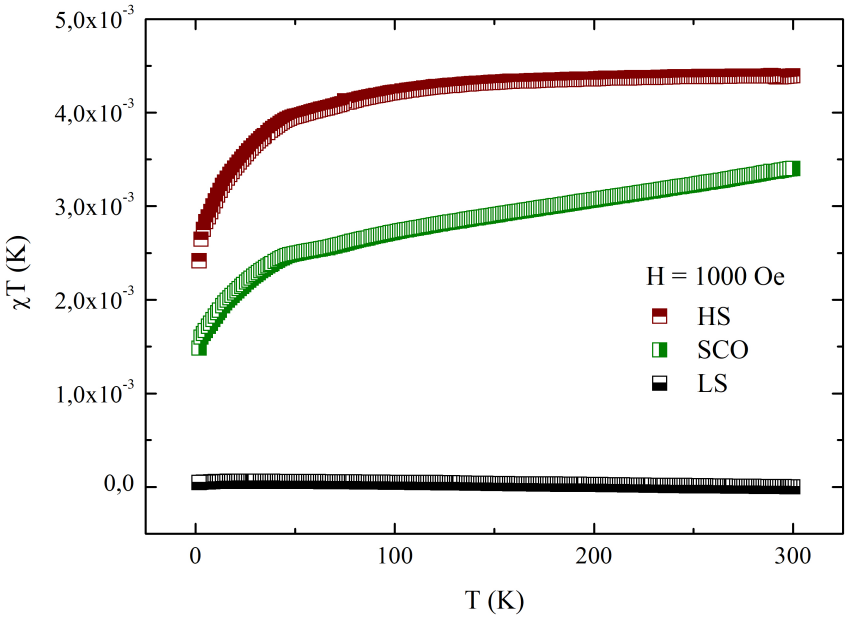

Figure 3.5: χT vs temperature for the three samples at $H = 1000$ Oe.

Following an initial growth at $T \leq 50$ K, which then becomes less steep between 50 K and 175 K, the HS system displays an almost constant χT at high temperatures, saturating at $\chi T \simeq 4.37 \cdot 10^{-3}$ K. The same holds for the LS compound, which exhibits positive values of χT, nearly constant throughout the investigated temperature range – apart from a small initial increase at $T \leq 20$ K of $\chi T \simeq 6.0 \cdot 10^{-5}$ K.

The very high and positive data of χT of the high-spin reference confirm that this compound is almost entirely composed of paramagnetic molecules, characterized by HS-Co(II) and a semiquinonate ligand.

On the other hand, the signal intensity of the LS reference is very weak with respect to the other samples, but is in line with the results obtained by the authors of Ref. [2]. In particular, we agree on an almost temperature-independent paramagnetic behavior. This may be constituted by low-spin molecules, or a residual component of HS molecules trapped in the LS-reference diamagnetic sample. Because, to our knowledge, the net spin of the LS sample molecules is not known yet, we cannot conclude

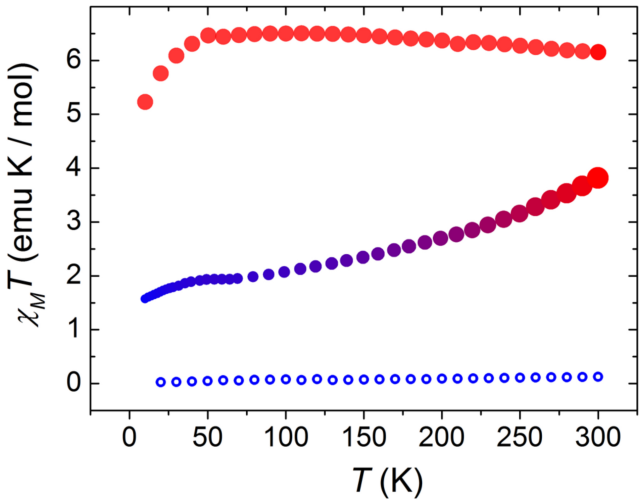

Figure 3.6: $\chi_M T$ vs temperature of the HS (red), SCO (blue-red, increasing) and LS (blue, empty) compounds in $H = 1000$ Oe. Reproduced from Ref. [2].

what the true magnetic state of this compound is.

The initial steep increase of χT observed in the HS data until T $\simeq$ 50 K, is also common to the SCO sample, and has already been reported by other authors in di-nuclear Cobalt-dioxolene compounds[2, 36]. Indeed, the excited multiplets of the $^4T_{2g}$ ground state of the HS-Co(II) ions become populated upon increasing temperature. The splitting in multiplets is due to symmetry distorsions and spin-orbit coupling of the octahedral HS moiety, as suggested by authors of Ref. [2].

The SCO compound does not follow a Curie-Weiss behavior: its χT increases with temperature, which is a sign that a spin-crossover transition is occurring. Consistently with what expected for Cobalt spin-crossover molecules (see, for instance, Chapter 1), the transition broadens over a wide range of temperatures. Also, similarly to what was observed for other thioeter-bridged valence-tautomeric dimers as in Ref. [2] and [12], the transition is not complete. This means that two plateaus at high and low temperatures are not observed, and the sample does not reach a net HS or LS state.

It is undeniable that the SCO complex has χT values much closer to those of the HS reference than the LS reference. We can therefore calculate the ratio

$$\%_{HS} = \frac{\chi_{SCO}}{\chi_{HS}} \tag{3.1}$$

of molecules which remain HS at a certain temperature, finding that this corresponds to 57 % at $T \simeq 50$ K, and 77 % at $T = 300$ K. A non-totality of LS molecules at low temperature is consistent with the 52 % percentage that the authors of [2] had found from their measurements of X-ray absorption spectroscopy. It indicates that the two radical ligands are not too strongly interacting, stabilizing the Cobalt ions in a fixed

oxidation state. This "negligible intramolecular cooperativity" had been observed in other spin-crossover solids and molecules displaying redox isomerism[2, 37].

On the other hand, the data collected in our SQUID experiments are not completely in agreement with those acquired by the authors of Ref. [2]. In Fig. 3.6 we report the product of molar magnetic susceptibility and temperature that they obtained as a function of temperature. The discrepancy in the curves found may be due to different sample preparation as well as the different experimental conditions.

3.4 Magnetization vs Magnetic Field

We acquired data of the magnetic moment of the three samples at a fixed temperature $T = 5$ K as a function of the external magnetic field, which ranges from negative (-600 Oe) to positive values ($5 \cdot 10^4$ Oe).

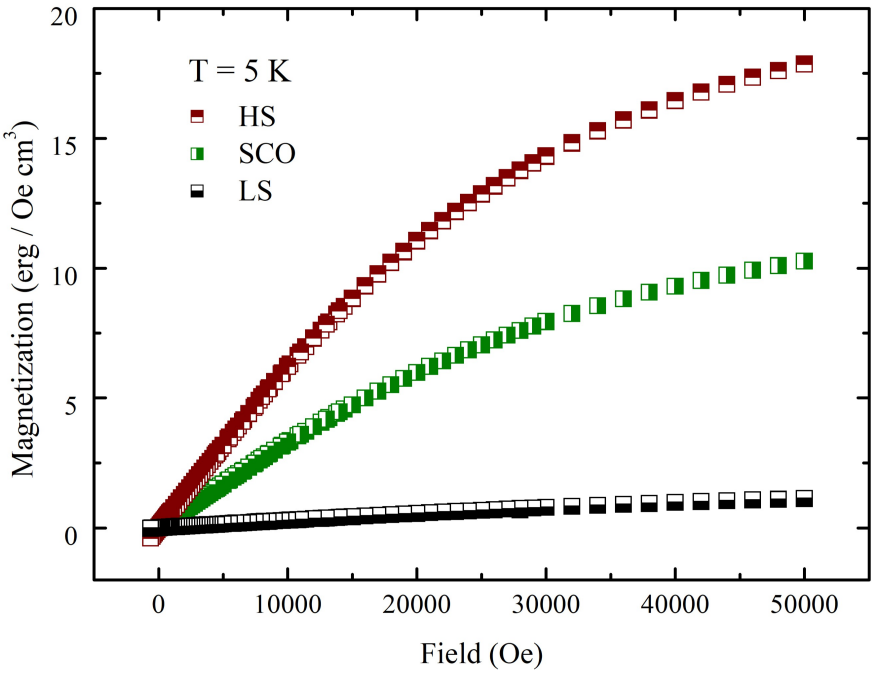

Figure 3.7: Magnetization vs magnetic field of the HS, SCO and LS samples, acquired at $T = 5$ K in a field range $-600 \leq H \leq 50000$ Oe.

As shown in Fig. 3.7, the magnetization of the samples increases with the applied field exhibiting a linear relationship $M \propto H$ for low field intensities ($H \leq 25$ kOe). The signal of the LS reference, again, is small compared to those of the SCO and HS compounds.

At higher field strengths, nonlinear contributions emerge, which are particularly pronounced for the SCO and HS compounds. This phenomenon can be attributed to the finite nature of the samples, which results in a discrete energy level structure. At low temperature, only the lower energy levels are populated, whereas at high temperatures or upon high applied magnetic fields, also the higher levels become populated.

On the other hand, if the sample were continuous and infinite, the energy levels would form a continuum, leading to a linear dependence of the magnetization upon external field, and the $M \propto H$ behavior would persist at all temperatures.

3.5 Summary

To conclude, this chapter has provided insights into the macroscopic magnetic behavior of the three thioeter-bridged Cobalt-dioxolene compounds. It has been established that both the high-spin and low-spin references exhibit a magnetic state characterized by temperature-independent paramagnetism, while the SCO sample undergoes a broad transition from a lower to a higher spin state.

The following chapter will be dedicated to the analysis of data obtained from NMR spectroscopy experiments.

Chapter 4

Nuclear Magnetic Resonance

We performed ^{1}H-NMR experiments on the three samples HS, SCO and LS at two fixed values of the external magnetic field $H = 1.4$ T and $H = 3.15$ T in the temperature range $4 \leq T \leq 305$ K.

We acquired data of the relaxation rates $1/T_1$, $1/T_2$ and spectra of the ^{1}H nuclear magnetization for each compound, studying them as a function of temperature and the applied magnetic field, and afterwards we compared the data obtained for the three samples. Whenever necessary, we also collected information on the stretching exponential (β) and the magnetization intensity derived from T_1 and T_2 measurements.

Contents

4.1 Spin-lattice Relaxation Rate

4.1.1 Bloembergen, Purcell, and Pound model

Following the discussion in Chapter 2, the Zeeman hamiltonian operator of the system of ^{1}H nuclei is often perturbed by a time-dependent operator $\hat{H}_P(t)$, which induces energetic transitions between the – in our case two – Zeeman levels. In a paramagnetic insulator, $\hat{H}_P(t)$ is primarily originated by the random time-fluctuations of electronic spins at every temperature. These can be associated with an effective local magnetic field $\vec{h}(t)$ such that:

$$\hat{H}_P(t) = \gamma\hbar\vec{I}\cdot\vec{h}(t) \tag{4.1}$$

In time-dependent perturbation theory, the stimulated transition rates $W_{\uparrow\downarrow}$ of the states aligned and anti-aligned to the field $\vec{H}_0$ can be expressed in terms of[27]

$$g(t) = \overline{\langle H_P(t)\cdot H_P(0)\rangle} \tag{4.2}$$

which is the autocorrelation function among the values of the perturbation at different times. If $g(t)$ has a time-dependence characterized by an exponential decay in time with correlation time τ_c, then the following formula holds true:

$$\frac{1}{T_1} = \frac{\gamma^2}{2}\int_{-\infty}^{+\infty} e^{i\omega_L t}\langle h_x(t)\cdot h_y(0)\rangle dt \tag{4.3}$$

This implies that $1/T_1$ is driven by the transverse components – i.e. perpendicular to the quantization axis – of the local fluctuating field at the nucleus, and is proportional to the Fourier-transform of the correlation function at the resonance frequency, also called "power spectrum" or "spectral density" of the correlation function[29].

In the specific case when $\langle h_x(t)\cdot h_y(0)\rangle = \langle\Delta h_\perp^2\rangle\exp\left(-\frac{t}{\tau_c}\right)$, then:

$$\frac{1}{T_1} = \frac{\gamma^2}{2}\langle\Delta h_\perp^2\rangle\frac{2\tau_c}{1+\omega_L^2\tau_c^2} \tag{4.4}$$

Also, when the fluctuations are isotropic, then $1/T_1 \sim 1/T_2$.

Three temperature regimes can here be identified. The first one is called the "fast-motions regime", where $\omega_L \ll 1/\tau_c$. In this case,

$$\frac{1}{T_1} = \gamma^2\langle\Delta h_\perp^2\rangle\tau_c. \tag{4.5}$$

The "slow motions regime" occurs when $\omega_L \gg 1/\tau_c$, and in this case

$$\frac{1}{T_1} = \frac{\gamma^2\langle\Delta h_\perp^2\rangle}{\omega_L^2\tau_c}. \tag{4.6}$$

The transition regime involves $1/\tau_c = \omega_L$ and $1/T_1$ displays a peak, whose value is

$$\frac{1}{T_1} = \frac{\gamma^2}{2}\langle \Delta h_\perp^2 \rangle \frac{1}{\omega_L}. \tag{4.7}$$

From simple considerations, the peak is expected when the characteristic frequency of the fluctuations matches the resonance frequency, i.e., $\omega_L \sim 1/\tau_c$.

All the models successfully employed in analyzing the data predict that the peak scales in amplitude and position as the magnetic field increases. Specifically, it shifts to lower intensities and moves towards higher temperatures with an increasing field strength[38]. This behavior was first investigated by Bloembergen, Purcell and Pound[39] on metallic solutions and has been verified in a variety of thermally activated processes for very different systems ever since[40, 41].

In the particular condition when the sample is a paramagnetic insulator, the longitudinal relaxation rate $1/T_1$ should be proportional to the mean square amplitude of the magnetic moment $\langle \mu^2 \rangle \sim \chi T$, thus the expression for $1/T_1$ assumes the specific form derived by Moriya[38, 42, 43]:

$$\frac{1}{T_1} = A' \cdot \chi T \cdot \frac{\tau_c}{1 + \omega_L^2 \tau_c^2} \tag{4.8}$$

where A' represents the geometric part of the hyperfine interaction.

Also, in many systems τ_c is thermally-dependent, and in most cases it has an activated Arrhenius-type dependence, such that

$$\tau_c = \tau_0 \cdot \exp\left(\frac{E_a}{k_B T}\right) = \tau_0 \cdot \exp\left(\frac{\Delta}{T}\right). \tag{4.9}$$

Here, E_a denotes the activation energy of the process, whereas $\Delta = E_a/k_B$. The quantity Δ can be estimated from the peak of $1/T_1$, as it roughly corresponds to the temperature at which the maximum relaxation rate is observed.

4.1.2 Spin-lattice Relaxation Rate vs Temperature

The ^{1}H spin-lattice relaxation rate, $1/T_1$, was derived from the recovery of nuclear magnetization following the experimental steps outlined in Chapter 2. The data were initially acquired for each sample over a wide range of temperatures ($8 \leq T \leq 300$ K).

Two external field strengths $H = 1.4$ T and $H = 3.15$ T were selected during our measurements. They were chosen to maximize the signal-to-noise ratio with respect to other fields (e.g. for $\omega_L = 100$ MHz). Then, a comparative evaluation of the three samples was made at each fixed field intensity. All the data acquired are reported in Fig. 4.1 and 4.2.

NMR measurements were performed under a low-frequency excitation condition, corresponding to $\omega_L \ll \omega_e$, where the second term represents the Heisenberg frequency associated with the exchange coupling constant between spins in a paramagnetic insulator[30]:

$$\omega_e = \frac{J}{\hbar}\sqrt{2z\frac{S(S+1)}{3}} \tag{4.10}$$

The two graphs are quite similar: the samples exhibit a sharp increase of $1/T_1$ at very low temperatures ($T \leq 20$ K). Then, a thermally activated behavior is seemingly observed in the spin dynamics in the temperature range $20 \leq T \leq 30$ K. As the temperature increases, the values of $1/T_1$ decrease, eventually stabylizing at a nearly constant value of $1/T_1 \simeq 10$ s^{-1} for the LS sample, and very similar values for the HS and SCO compounds, such as $1/T_1 \simeq 150$ s^{-1} both in $H = 1.4$ T and $H = 3.15$ T.

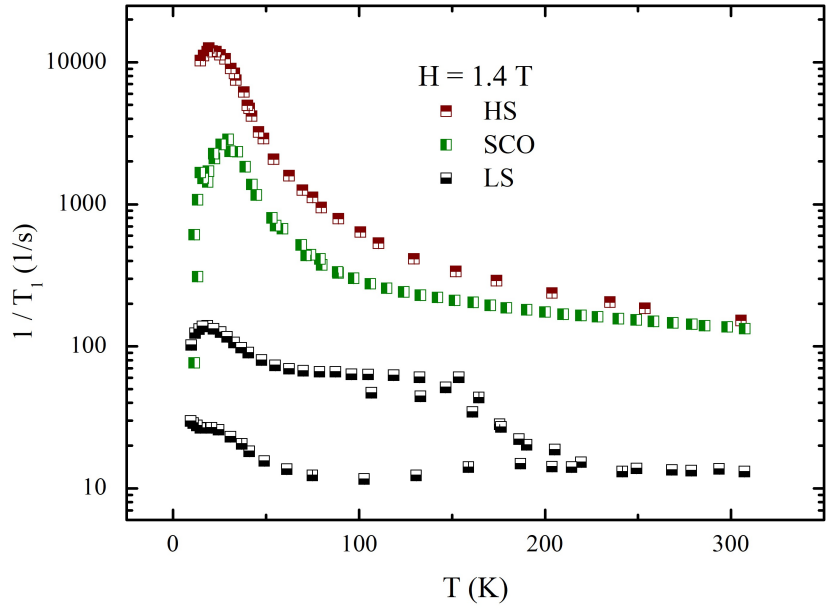

Figure 4.1: $1/T_1$ vs temperature for the compounds HS, LS and SCO in $H = 1.4$ T.

The $1/T_1$ peak data of the three samples span different orders of magnitude. While the signal of the HS reference reaches $1/T_1 \simeq 10^4$ s^{-1}, the peak occurs at $1/T_1 \simeq 2.85 \cdot 10^3$ s^{-1} for the SCO compound and at $1/T_1 \simeq 2.3 \cdot 10^1$ s^{-1} for the LS sample. The maximum relaxation rate of the SCO compound is intermediate between the HS and the LS reference values, but it is closer to that of the HS compound by one order of magnitude.

The thermally-activated behavior could be consistent with a Bloembergen-Purcell-Pound model[39], adapted to the Moriya law,[42, 43] – valid for the relaxation in param-

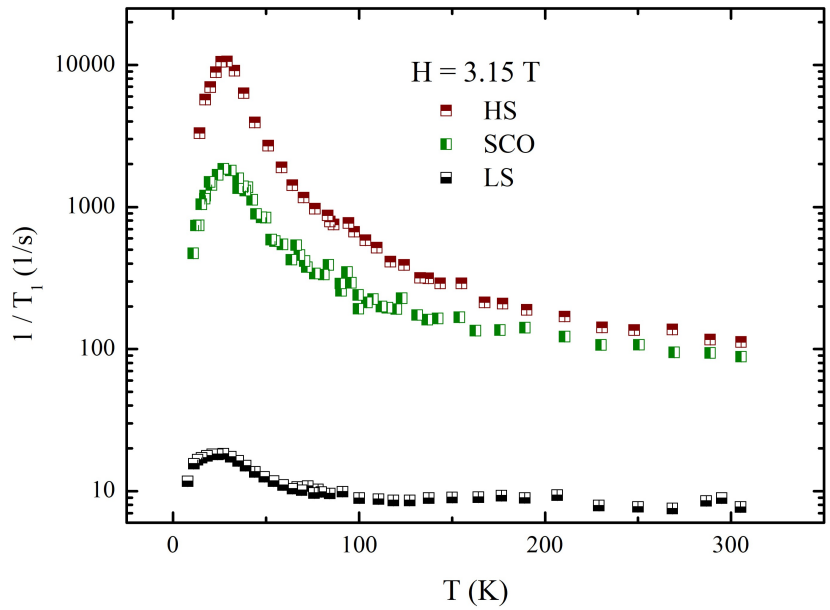

Figure 4.2: $1/T_1$ vs temperature for the compounds HS, LS and SCO in $H = 3.15$ T.

agnets – with an Arrhenius-type relationship of the correlation time:

$$\frac{1}{T_1} = A' \cdot \chi T \cdot \frac{\tau_0 \exp\left(\frac{\Delta}{T}\right)}{1 + \omega_L^2 \tau_0^2 \exp^2\left(\frac{\Delta}{T}\right)} \tag{4.11}$$

Accordingly, we report all the data collected for the SCO compound at two field strengths, together with their relative BPP fit based on Eq. 4.11, in Fig. 4.3.

In general, the Bloembergen-Purcell-Pound (BPP) model is based on the assumptions of a single correlation frequency and that both A' and τ_0 are field-independent. In this limit, the height of the $1/T_1$ peak should be proportional to H_0^{-1} and the peak position should scale to higher temperatures as the field increases. This is a common feature of many single molecule magnets as well as single ion magnets[38].

What we observe, instead, is that the activation energy of the process Δ does not depend on the field intensity for any sample, obtaining $\Delta \simeq 113$ K for the HS and SCO compounds, and $\Delta = 36$ K for the LS reference.

Such similar values of Δ for the SCO and HS compounds indicate a major abundance of HS-Co(II) centers within the SCO sample, and are consistent with the close similarity of the SCO with the HS sample SQUID data throughout the total investigated temperature range.

As for the interpretation, Δ can be associated to the energy required to populate the first available electronic levels, that is, the energy of the first molecular excited

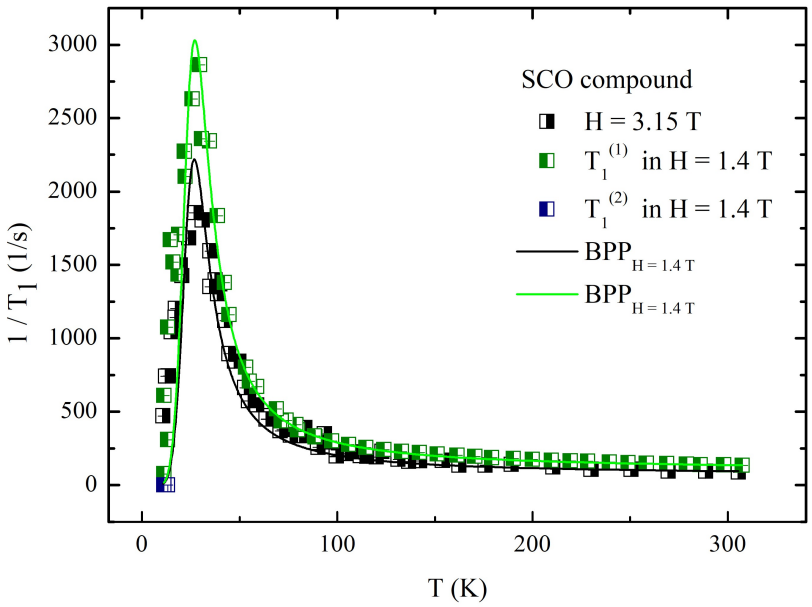

Figure 4.3: Data of $1/T_1$ vs temperature of the SCO compound in $H = 1.4$ T and $H = 3.15$ T. The lines are the BPP fitting models.

state. Therefore, we attribute this value to the population of the excited multiplets of the $^4T_{2g}$ ground state of the HS-Co(II) centers, as suggested by the authors of Ref. [2]. The application of a magnetic field does not influence the energetic disposition of orbitals, because Δ does not vary with the field strength. Lastly, the activation temperature is consistent with the initial increase of χT observed in the DC SQUID experiments.

On the other hand, the height of the $1/T_1$ peak, given by the maximum spin-lattice relaxation rate A', acquires a smaller value upon application of a smaller field strength. However, it spans $A' \simeq 10^{12}$ s^{-1} for the SCO compound, $A' \simeq 10^{13}$ and $\simeq 10^{10}$ s^{-1} for the HS and LS references, respectively. Correspondingly, the times τ_0 tend to increase upon lowering the field, but still they are not dramatically different for the three samples ($\tau_0 \simeq 10^{-11}$ s for the HS and SCO compounds, while $\tau_0 \simeq 10^{-10}$ s for the LS reference).

Remarkably, below $T \leq 15$ K, the recovery of ^{1}H nuclear magnetization of this sample in $H = 1.4$ T was no longer a stretched exponential, and two distinct trends with $\beta_1 = \beta_2 = 1$ were observed – see, for instance, Fig. 2.13 in Chapter 2. This is why we have reported some blue points in the lower part of the graph: these correspond to the second group of nuclei relaxing with a different T_1. However, only the first data set was employed for the fitting procedure using the BPP model.

The dependence, although not marked, of A' and τ_0 on the applied field strength in our experiments is coherent with the lack of scaling of the $1/T_1$ on the field intensity, and also with the lack of proportionality of $1/T_1$ on the χT[38]. To prove it, we derived the following ratio:

$$\frac{1}{T_1 \cdot \chi T} = A' \cdot \frac{\tau_0 \exp\left(\frac{\Delta}{T}\right)}{1 + \omega_L^2 \tau_0^2 \exp^2\left(\frac{\Delta}{T}\right)} \tag{4.12}$$

The data of χ were acquired by SQUID magnetometry (see Chapter 3) at two different field intensities $H = 1000$ Oe and $H = 14000$ Oe and are reported in Fig. 4.4. In the analysis of the $1/T_1$ data, though, we made use of the low-field χ for the determination of the spectral density of electronic fluctuations for two main reasons. Firstly, the values of χ are almost identical in the two field strengths (see Fig. 4.4) and, secondly, it was easier to acquire data also for the background, which were then subtracted from those of the three samples.

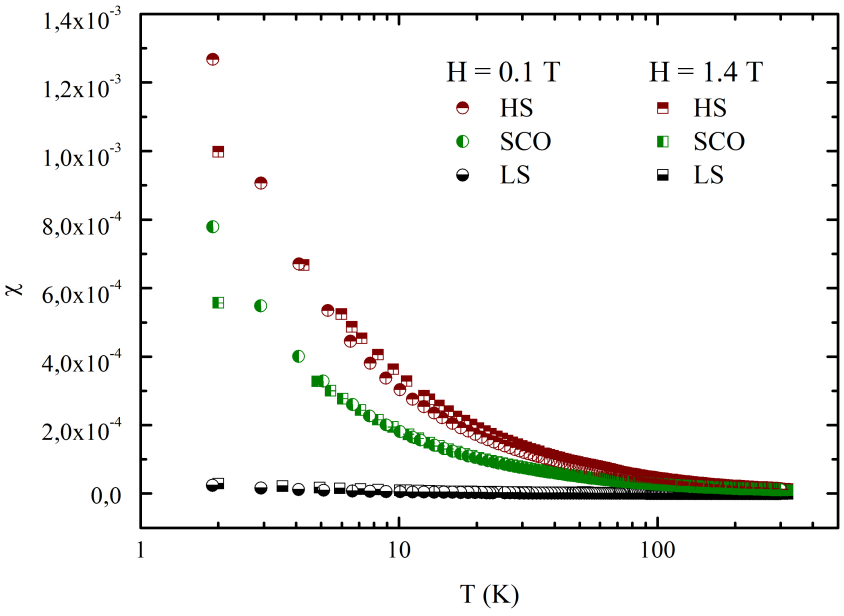

Figure 4.4: Magnetic susceptibility vs temperature of the HS, SCO and LS samples added to their background contributions, at $H = 0.1$ T and $H = 1.4$ T.

The scaling of the $1/T_1$ data with χT according to Eq. 4.12 is reported in Fig. 4.5. Ignoring the increase of $1/(T_1 \chi T)$ at high temperatures of the LS sample – which is a result of the rapid decrease of χT towards T $\simeq$ 300 K encountered in SQUID experiments, implying an imperfect subtraction of the background contribution from the

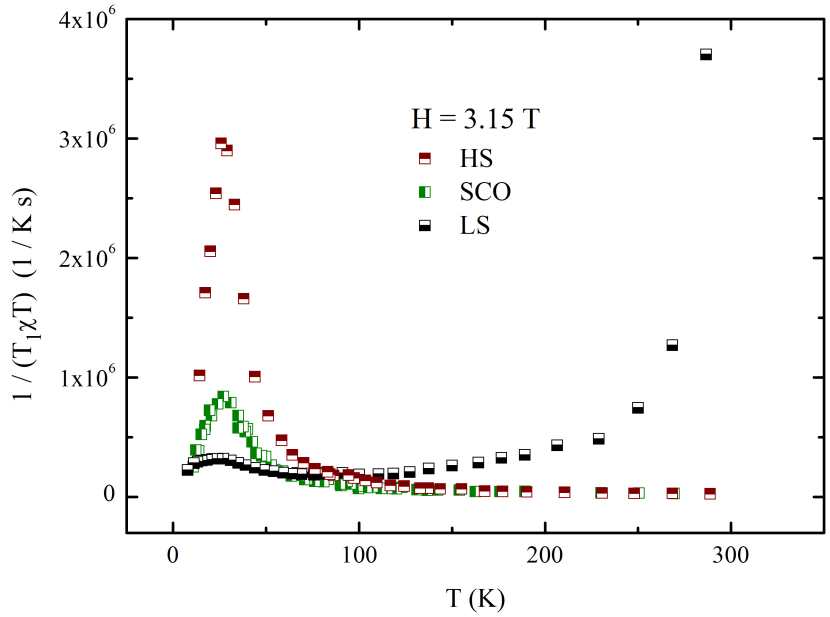

Figure 4.5: $1/(T_1\chi T)$ vs temperature of the HS, SCO and LS samples at $H = 3.15$ T.

experimental data – the data of $1/T_1$ of the HS and SCO at high temperatures are linearly proportional on χT. The two samples behave quite similarly and have the same substantial magnitude of $1/T_1\chi T$ in both external field values. We can therefore conclude that the principal relaxation mechanism at high temperatures is the electronic paramagnetism.

4.1.3 Stretching Parameter

β is a phenomenological "stretching" parameter accounting for a distribution of T_1 values, and the data of β can also provide useful information on the internal dynamics of the molecules. As an example, we report the β data obtained for the three samples in an external field $H = 1.4$ T upon lowering the temperature in Fig. 4.6

The values of β of the three compounds are nearly constant at high temperatures, with $\beta \simeq 0.95$, indicating that the ^{1}H inside the samples are all equivalent and perceive the same environment. Referring to the SCO and HS samples, in correspondence with the increase of $1/T_1$, a reduction of β is observed, suggesting that the nuclei are no longer equivalent: those near the Cobalt centers perceive the onset of population on the energy levels and the variation of local magnetic field, whereas those farther do not. As a consequence, the decay results in a stretched exponential, with $\beta \leq 1$.

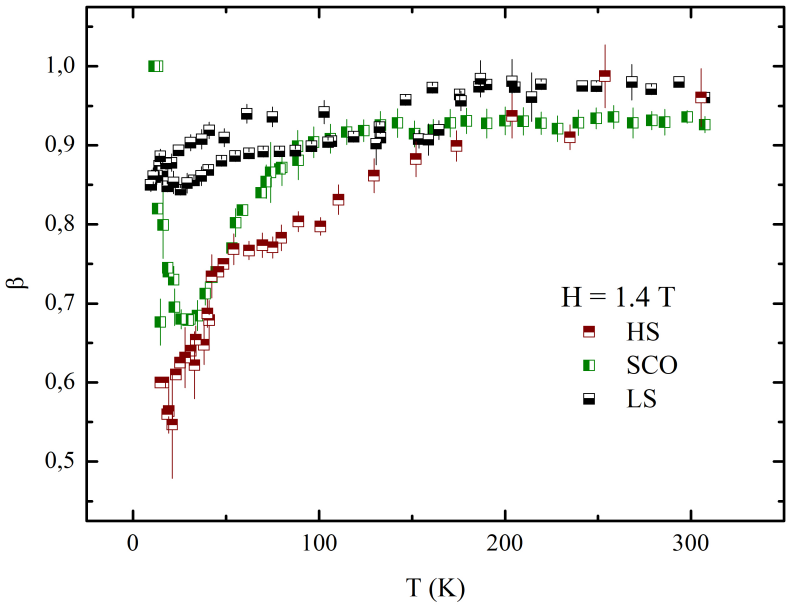

Figure 4.6: β values acquired from measurements of $1/T_1$ vs temperature for the compounds HS, LS and SCO in H = 1.4 T.

4.1.4 LS Reference

The behavior of the LS system is rather unusual. In Fig. 4.7 we have reported its $1/T_1$ as a function of temperature at the two field intensities $H = 1.4$ T and $H = 3.15$ T.

Referring to the field strength $H = 1.4$ T, two trends emerge (black squares). In both, for $T \geq 180$ K, the $1/T_1$ values match and are also consistent with those measured at $H = 3.15$ T at the same temperature range. At $T \simeq 180$ K, a small peak appears, followed by a slight decrease in $1/T_1$ and a more pronounced peak as the temperature decreases.

The seemingly activated trend at $T \simeq 180$ K has also been reported by other authors[9]. In this case, the slight dependence of the peak temperature and intensity may suggest low-frequency diffusive spin fluctuations or some internal molecular motions. The analysis of the second peak, on the other hand, has been presented in the previous paragraph: the activation energy Δ of the thermally-activated process corresponds to $\Delta = 36$ K, indicating that the energy splitting resulting from the octahedrally coordinated system differs from that of the other two compounds. This indicates that the LS reference is mostly composed of molecules in which cobalt exists in the LS-Co(III) oxidation state, while the other samples display a prevalent HS-CO(II).

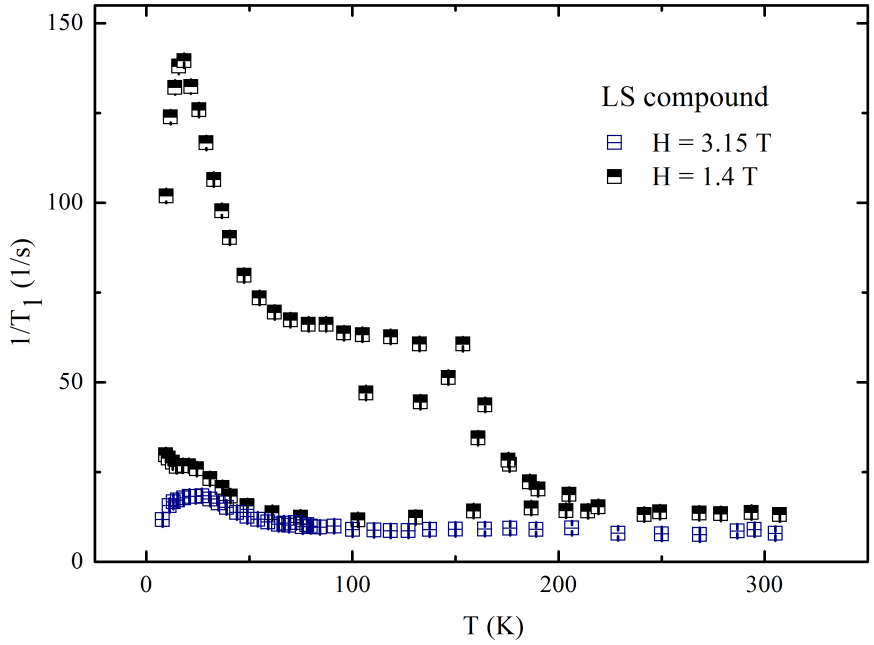

Figure 4.7: $1/T_1$ vs temperature data for the LS sample in H = 1.4 T (black) and H = 3.15 T (blue).

During the course of the experiment, we initially performed a field-cooled-cooling (FCC), which means that, after applying the magnetic field, the data were acquired while decreasing temperature. This was followed by a field-cooled-warming (FCW), during which data were acquired with field on while heating the sample. We report the procedure followed in Fig. 4.8 for clarity.

Because two slightly different paths were observed, we decided to repeat a FCC measurement to replicate the initial trends. However, this behaviour was not reproducible: the values of $1/T_1$ varied upon different cooling protocols used and this discrepancy suggests a dependence on thermal history. This may account for a spin-glassy behavior, which is a disordered magnetic state characterized by competing interactions but, in principle, a spin-glassy behavior can be detected by SQUID as well, through similar FC-ZFC protocols. However, our SQUID measurements did not reveal any anomalous trends, and the data coincided within the experimental error.

We then suggest that the observed behavior could be owed to some metallic impurities trapped within the sample. For their investigation, we performed a rapid cooling procedure, to ensure that the data were on the lowest-lying branch, and we studied the curve $I(0)$ at fixed temperature ($T = 120$ K) as a function of the time. We aimed to determine whether any ferromagnetic behavior was present, which would have re-

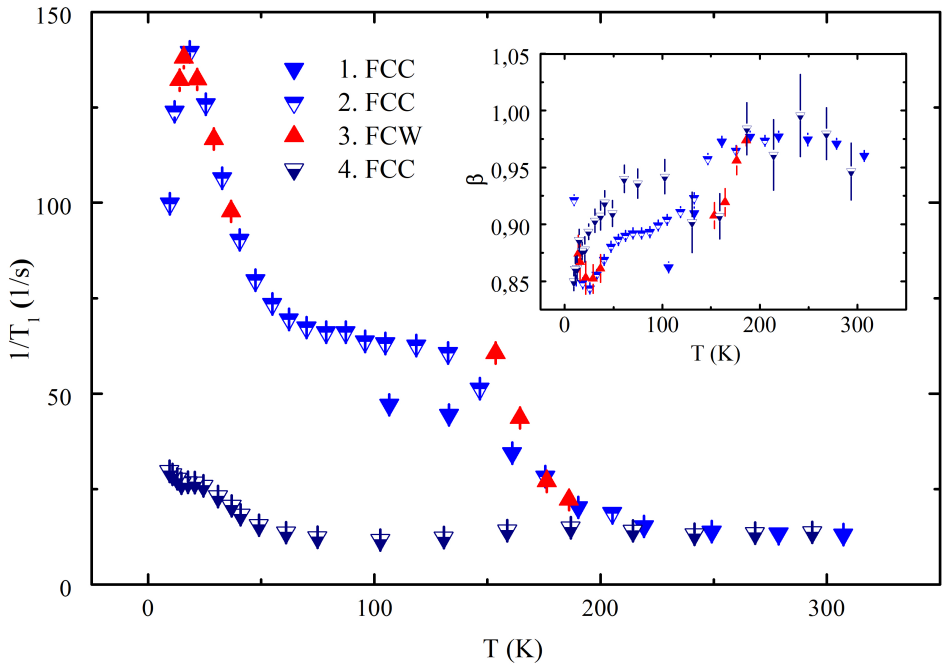

Figure 4.8: $1/T_1$ vs temperature data of the LS sample in H = 1.4 T. Inset: β derived from T_1 measurements.

sulted in a modification of $1/T_1$ over time, but nothing changed, leading to the conclusion that the magnetic susceptibility $\chi \propto 1/T_1$ is substantially time-independent and therefore this sample is non-magnetic. The phenomenon was not fully reproducible and requires further investigation. From a comparison with the data of the HS and SCO samples, it is plausible that the real trend of the LS reference is the lowest-lying branch, while the highest one can be attributed to a ferromagnetic impurity.

4.2 Spectral Linewidth

We collected data of the ^{1}H NMR spectrum, in order to subsequently derive the spectral linewidth, which can provide useful insights on the electronic state of a sample.

The spectrum was best fitted according to a Voigt profile[44], which is the convolution of a Gaussian and a Lorentzian function. The full width at half maximum (FWHM or Γ) of the curve was extracted, as given by the following formula:

$$\Gamma_{Voigt} = 0.5346 \cdot \Gamma_L + \sqrt{(0.2166 \cdot \Gamma_L^2) + \Gamma_G^2} \tag{4.13}$$

The spectral linewidths of the three compounds in $H = 1.4$ T and $H = 3.15$ T as a function of temperature are reported in Fig. 4.9 and 4.10. We observed a major inhomogeneous broadening at every temperature, which increases upon decreasing temperature, resulting in a seemingly linear graph obtained at $H = 3.15$ T. For $H = 1.4$ T the linear trend is lost primarily for the SCO and HS compounds.

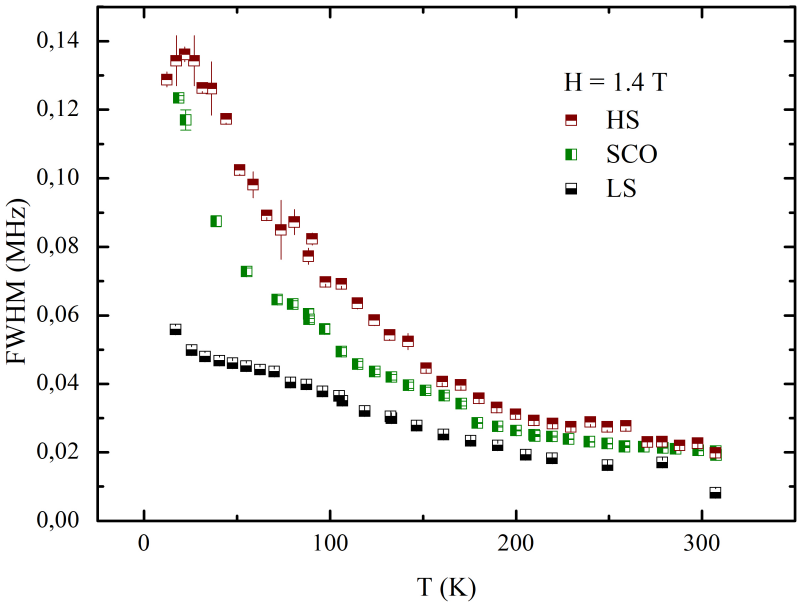

Figure 4.9: Linewidth vs temperature of the three compounds at $H = 1.4$ T.

This behavior can be clarified through the following considerations. At high temperature, the local magnetic fields induced by the paramagnetism of the samples are randomly fluctuating and all protons, both near and far from the Cobalt magnetic centers, are equivalent, such as they perceive the “mean value” of the magnetic field

around them. As a consequence, the decay is an exponential and thus the spectrum can be conveniently fitted through a Lorentzian curve. This mechanism is known as "exchange-narrowing".

On the other hand, at low temperatures, a spontaneous distribution of quasi-static local magnetic fields emerges, and is owed to electronic spins which interact with other electrons and nuclei[38]. This mechanism is mostly isotropic.

As a result, although a Voigt profile was employed for the fitting procedure, we observed a temperature-dependent variation in the spectral weights of the gaussian and lorentzian lineshapes. At high temperature, the lorentzian lineshape was predominant, while at low temperature ($T \leq 130$ K), it turned to a gaussian profile.

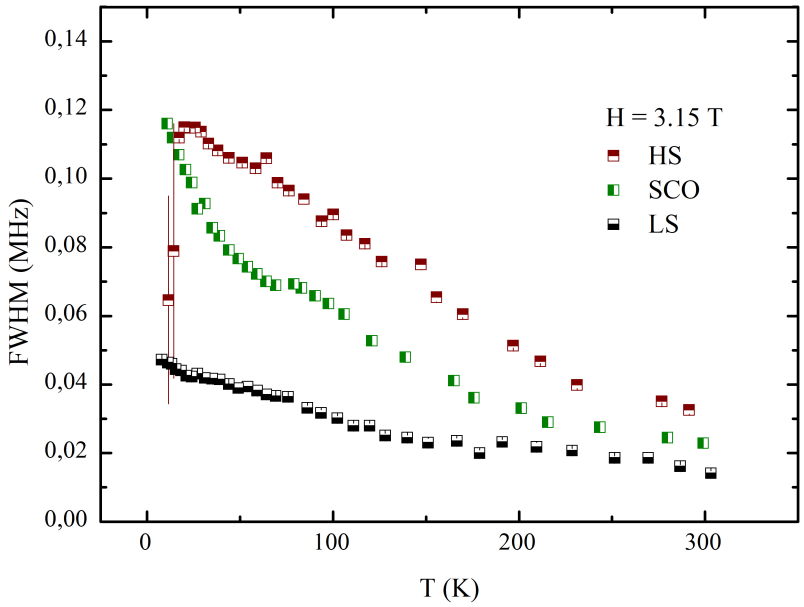

Figure 4.10: Linewidth vs temperature of the three compounds at $H = 3.15$ T.

4.3 Spin-spin Relaxation Rate

The spin-spin relaxation rate $1/T_2$ was acquired following the procedure outlined in Chapter 2. We also collected data of the echo signal amplitude A, which is proportional to the magnetization M_{xy} which decays on the transverse plane producing the echo

signal. In detail, we can consider that:

$$M(2\tau_{echo}) = M_{xy} \cdot \exp\left\{\left[-\left(\frac{2\tau}{T_2}\right)^{\beta}\right]\right\} \tag{4.14}$$

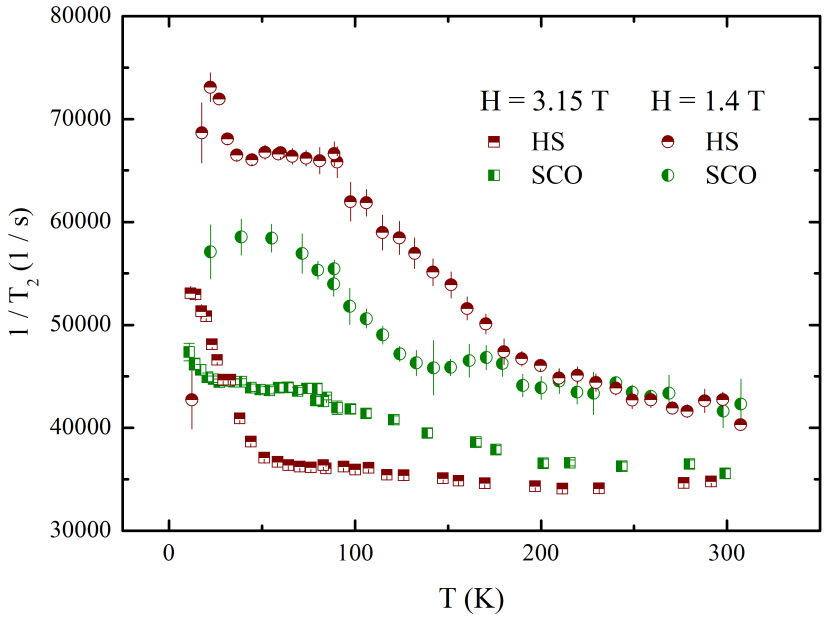

Figure 4.11: Spin-spin relaxation rate vs temperature of the compounds HS and SCO at two field values.

From the SCO and HS data, reported in Fig. 4.11, the spin-spin relaxation rate shows an increase upon lowering the temperature, which results in a peak at $T \leq 100$ K. The data acquired at two field intensities are comparable, and even exhibit a superposition and inversion of the signals for the two samples. However, this is attributed to the experimental resolution, and can not be due to the intrinsic compounds, because it would have resulted in a similar behavior also in the FWHM.

On the other hand, some major issues were encountered while acquiring data for the LS reference, mostly due to technical inadequacy in providing short time scales to offer a complete relaxation curve for this sample. As a result, the data appeared to be very irregular and scattered, and thus were not reliable.

The values of M_{xy} were subsequently plotted as a function of the temperature. The ^{1}H signal amplitude of both samples display an almost constant value of $A \simeq 6.0 \cdot 10^4$ upon applied field strength $H = 3.15$ T and $A \simeq 9.0 \cdot 10^4$ upon field strength $H = 1.4$

T. Also, it rapidly increases between $50 \leq T \leq 100$ K and displays a sharp drop below $T \simeq 50$ K. This significant decrease at low temperatures is known as "wipe-out effect", and is typical of many single-molecule magnets and spin-glassy systems[45, 46].

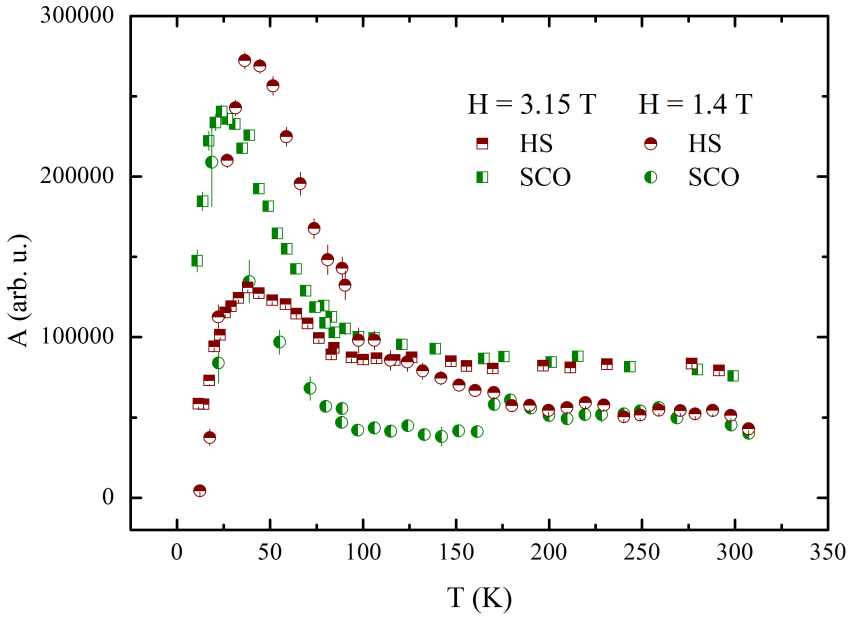

Figure 4.12: Amplitude of the T_2 signal vs temperature of the HS and SCO compounds.

The wipe-out effect is principally due to the increase of the spin-lattice and spin-spin relaxation rates occurring at $20 \leq T \leq 50$ K. The one we observe is of the "dynamical case" which means that at low temperatures the nuclear spins couple to the slowly fluctuating magnetic local fields, which are then perceived as a second static magnetic field. The relaxation times T_1 and T_2 become so short that the transverse component of the magnetization decays irreversibly before it can be seen through an NMR pulse experiment[45, 47].

4.4 Summary

In conclusion, in this chapter we have presented our results of ^{1}H NMR spectroscopy experiments performed at two field intensities over a wide range of temperatures.

The relaxation rate $1/T_1$ has provided insight on the internal dynamics and the population onset of the energy levels, while the linewidth and the relaxation rate $1/T_2$ brought information about the fluctuating local magnetic fields at the nuclear sites.

Conclusions

In this thesis, we have discussed the magnetic properties of three Cobalt-dioxolene compounds using Nuclear Magnetic Resonance and DC SQUID magnetometry.

The SQUID magnetometry could provide insights on the static magnetic macroscopic properties of the three samples. In detail, our experimental results highlight a spin state (paramagnetic) almost independent upon temperature variations for the HS and LS references, with a very high value of $\chi T \simeq 4.38 \cdot 10^{-3}$ (emu K / Oe cm^3) for the first and a value smaller by two orders of magnitude for the latter. The value of the net spin remains unknown due to the not yet determined exchange coupling constant between ligands and metal atoms.

On the other hand, the SCO sample displays a valence-tautomeric spin-crossover transition, which was expected from previous examples in literature. This transition is gradual, covering a wide temperature range, and is incomplete, meaning the compound does never reach a stationary magnetic state. However, it is evident that the sample is predominantly composed of HS molecules at every temperature.

We also presented our ^{1}H NMR measurements over a $8 \leq T \leq 300$ K temperature range at two fixed esternal field strengths. The analysis of $1/T_1$ as a function of temperature reveals that, irrespective to the applied magnetic field, all the samples display a thermally-activated behavior at $20 \leq T \leq 30$ K. Through a Bloembergen-Purcell-Pound model we could define that this consists of the population onset of the excited states. The LS reference sample is almost entirely composed of molecules in which Cobalt exists in the LS-Co(III), while the other samples display mostly HS-Co(II) centers. Thus, the distribution of electronic orbitals results in a lower energy splitting of the ground and excited states for the LS sample with respect to the SCO and HS samples. For the LS compound, a thermally activated process associated with internal molecular motions is also observed at approximately $T \simeq 180$ K.

From the analysis of the nuclear spin-spin relaxation rate $1/T_2$ and spectra, we were able to infer that, at low temperature, quasi-static local magnetic fields emerge, resulting in a broader linewidth and an increased $1/T_2$. However, at high temperatures, the electronic dynamics is activated, thus resulting in exchange-narrowing in the spectral linewidths. Also, the spectral density of electronic fluctuations confirms that the paramagnetism of the samples drives the nuclear relaxation at high temperatures.

Acknowledgments

May the reader forgive me if the acknowledgments will be held in italian language.

I miei più sentiti ringraziamenti sono rivolti ai professori Giacomo Prando e Alessandro Lascialfari, per la loro continua disponibilità e pazienza, anche nei giorni di sabato e domenica e nelle lunghe notti di giugno in fase di consegna del progetto di dottorato.

Ringrazio molto Giacomo per avermi insegnato il mestiere del ricercatore in laboratorio, ed avermi sempre spiegato tutto nei minimi dettagli in modo chiaro e ordinato, rispetto all'entropia che c'era intorno a noi.

Ringrazio il prof. A. Lascialfari, perchè nonostante i suoi 10^6 impegni riesce sempre a trovare un momento libero per aiutarmi, anche quando io, eroicamente, penso di non averne bisogno.

Desidero ringraziare calorosamente anche gli altri due membri del gruppo di ricerca, il professor P. Carretta e la ricercatrice Francesca Brero, che mi hanno assistito e consigliato in fase di presentazione dei risultati di tesi e del progetto di dottorato.

Rinnovo i miei ringraziamenti della scorsa tesi verso tutti coloro che mi hanno sostenuto e aiutato in questo percorso, ognuno di loro sa il perché.

Infine, per il lettore, *in quanto a questa tesi, se non v'è dispiaciuta affatto, vogliatene bene a chi l'ha scritta, e anche un pochino a chi ve l'ha raccontata, che qualora fossimo riusciti di annoiarvi, credete bene che non s'è fatto apposta.*[48]

Bibliography

[1] G. K. Gransbury, *et al.*, *J. Am. Chem. Soc.*, 142, 10692-10704 (2020)
[2] G. Poneti, M. Mannini *et al. Inorg. Chem.*, 52, 20, 11798-11805 (2013)
[3] I. Krivokapic *et al.*, *Coord. Chem. Rev.*, 251, 3-4, 364-378 (2007)
[4] P. Gutlich and J. Jung, *Jour. of Mol. Str.*, 347, 21-38 (1995)
[5] A. Abragam, B. Bleaney, *Electron Paramagnetic Resonance of Transition Ions*, Oxford University Press (1970)
[6] R. M. White, *Quantum theory of magnetism – 2nd edition*, Springer (1983)
[7] C. Schaller, *LibreTexts, 2.8, Ligand Field Theory*
[8] T. Tezgerevska *et al.*, *Coord. Chem. Rev.*, 268, 23-40 (2014)
[9] F. Caracciolo *et al. Phys. Rev. B*, 98, 5, 054416 (2018)
[10] L. Lobato, *et al. Dalton Trans.*, 53, 9933 (2024)
[11] P. Raithby *et al.*, *Inorg. Chem.*, 60, 12, 8665-8671 (2021)
[12] T. Fischer *et al.*, *Dalton Trans.*, 53, 3104 (2024)
[13] M. Nihei *et al.*, *Coord. Chem. Rev.*, 251, 2606-2621 (2007)
[14] M. Cowan *et al.*, *J. Am. Chem. Soc.*, 134, 2892-2894 (2012)
[15] J. Zarembowitch and O. Kahn, *Inorg. Chem.*, 23, 589-593 (1984)
[16] E. Konig and G. Ritter, *Solid State Commun.*, 18, 279 (1976)
[17] E. Muller *et al.*, *Chem. Phys. Lett.*, 93, 567 (1982)
[18] G. K. Gransbury, *PhD thesis* (2020)
[19] G. Gransbury *et al.*, *Chem. Sci.*, 10, 8855 (2019)
[20] Y. Suenaga *et al.*, *Inorg. Chem.*, 44, 6183-6191 (2005)
[21] A. Beni *et al.*, *Chem. Eur. J.*, 14, 1804-1813 (2008)
[22] G. Poneti *et al.*, *Angew. Chem. Int. Ed.*, 49, 1954, (2010)
[23] O. Sato *et al.*, *S. Acc. Chem. Res.*, 40, 361 (2007)
[24] K. Chen *Intern. J. Mol. Sci.*, 21, 5666 (2020)
[25] E. Fukushima and S.B.W. Roeder, *Experimental Pulse NMR* (1981)
[26] R. Lu *et al.*, *Master thesis – "Problemi di dinamica di spin in sistemi magnetici a bassa dimensionalità"*, (1977)
[27] C.P. Slichter, *Principles of Magnetic Resonance – 3rd edition*, Springer (1990)
[28] E. Deleporte *et al.*, *Résonance Magnétique Nucleaire*
[29] G. Jug, *Instr. Sci & Techn.*, 45, 3, 324-337 (2016)

[30] P. Carretta, *A short introduction to Nuclear Magnetic Resonance*
[31] T. Kremer, *Surveys in Geophysics*, 43, 1-55 (2022)
[32] S. Mugiraneza *et al.*, *Comm. Phys.*, 5, 95 (2022)
[33] A. Kraft *et al.*, *UBC Physics 502 Project* (2017)
[34] R. Black and F. Wellstood, *The SQUID handbook: Applications of SQUIDs and SQUID Systems*, 2, 391-440 (2006)
[35] *MPMS Application note 1014-210, Quantum Design*
[36] K. Alley *et al. J. Am. Chem. Soc.*, 135, 8304 (2013)
[37] A. Dei *et al. Inorg. Chem.*, 49, 3271 (2010)
[38] E. Luccacini *et al. Phys. Rev. B*, 100, 174416 (2019)
[39] N. Bloembergen *et al.*, *Phys. Rev.* 73, 7, (1948)
[40] D. Opherden *et al.*, *Phys. Rev. B*, 103, 014428 (2021)
[41] G. Prando *et al.*, *Phys. Rev. Mat.*, 7, 094002 (2023)
[42] T. Moriya, *Progr. theor. Phys.*, 16, 23 (1956)
[43] T. Moriya, *Progr. theor. Phys.*, 28, 371 (1972)
[44] E. E. Whiting, *J. Quant. Spectrosc. Radiat. Transfer.* , 8, 1379-1384 (1968)
[45] A. Lascialfari *et al. Phys. Rev. B*, 82, 134403 (2010)
[46] M. Belesi *et al. Phys. Rev. B*, 72, 014440 (2005)
[47] M. Isah *et al.*, *Phys. Rev. B*, 111, 014444 (2025)
[48] A. Manzoni, *I Promessi Sposi*, (1842)